Spin-Orbit Torque Switching of Magnetic Tunnel Junctions by Oxide Material

CNF Project Number: 111-80

Principal Investigator(s): Robert A. Buhrman

User(s): Arnab Bose

Affiliation(s): Applied and Engineering Physics, Cornell University

Primary Source(s) of Research Funding: Department of Defense-Intelligence Advanced Research Projects Activity

Contact: buhrman@cornell.edu, ab2729@cornell.edu

Primary CNF Tools Used: 5x stepper, AJA sputtering, ASML, JEOL 6300, Oxford

Abstract:

Generation of spin-orbit torques (SOT) has remained one of the major aspects of spintronics for the past decade [1]. It has been shown that SOT can be efficiently created by the heavy metals such as Pt, Ta, W [1] and with their alloys [1]. It can be useful for magnetic memory application [1-2]. We recently studied SOT in oxide-based systems such as $SrRuO_3$ [2], IrO_2, etc. We aimed to implement switching of magnetic tunnel junctions (MTJ) using the intrinsic spin Hall effect of oxide materials.

Summary of Research:

To quantify SOT, the spin torque ferromagnetic resonance (ST-FMR) technique is used [1]. Basic device structure of an ST-FMR device and an MTJ are shown below (Figures 1 and 2). ST-FMR devices are fabricated by two-step optical lithography processes. Initially optical lithography is done on a film consisting of a ferromagnet/non-magnet bi-layer, followed by Ar-ion milling and lift off process. Another step of optical lithography is done to make contact pads on the small micron size devices, which also involves sputtering and lift-off process. The CNF 5x stepper is used for optical lithography and contact metallization is done by CNF-AJA sputtering instrument. MTJ fabrication is very complex and involves many steps — i.e. sputtering the MTJ film --> optical lithographys to make the channel (ASML) --> etching the channel --> lift off the resist --> electron-beam lithography (JEOL 6300)+plasma etching (Oxford) to make a pattern of the MTJ pillar on the channel --> selective Ar-ion etching to remove other material apart from the non-magnetic base or heavy metal --> SiO_2 evaporation (even hour evaporator) --> lift off the resist --> final layer of optical lithography (ASML) for contact pad patterning --> sputtering Ti(5nm)/Pt(60nm) by AJA at CNF --> lift off. Characterization of the device fabrication is monitored by tapping mode AFM to confirm the existence of the channel and the pillar. Detailed method of the device fabrication can be found in reference [1]. Our devices are aimed to operate for fast and reliable magnetic memory application.

References:

[1] L. Liu, et al., Science 336, 555 (2012) and citations of this paper.

[2] Y. Ou, et al., NanoLetters 19, 63663-3670 (2019).

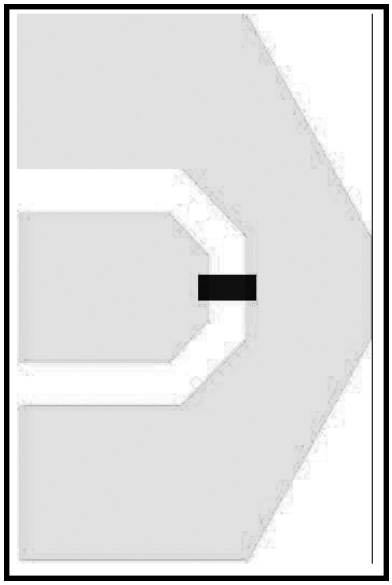

Figure 1: Schematics of an ST-FMR device.

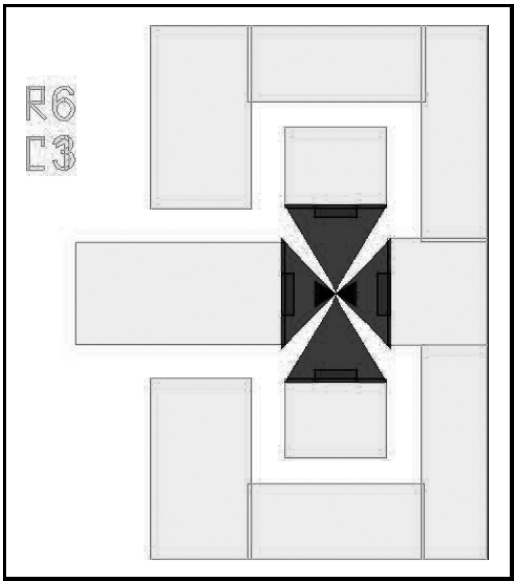

Figure 2: Schematics of an MTJ.

Reducing Write Current of Three Terminal Magnetic Tunnel Junctions by Engineering the Spin Hall Channel Structures

CNF Project Number: 111-80

Principal Investigator(s): Robert A. Buhrman

User(s): Shengjie Shi

Affiliation(s): Applied and Engineering Physics, Cornell University

Primary Source(s) of Research Funding: Department of Defense -Intelligence Advanced Research Projects Activity

Contact: buhrman@cornell.edu, ss2882@cornell.edu

Primary CNF Tools Used: ASML, JEOL e-beam 6300FS, Veeco AFM

Abstract:

Three terminal magnetic tunnel junctions (MTJs) are very good candidates for future cache memory applications due to their low energy consumption, fast switching characteristics, and reliable operation. To demonstrate the practicality of these structures being used in high density memory arrays, further reduced switching current is desired. In this report we show that by re-designing the layout of the spin Hall channel that is used to supply spin current that switches the MTJs, we can obtain significant reduction in switching voltage thanks to a dramatic decrease in the channel resistance caused by shortened length and a faster spread-out.

Summary of Research:

One of the key advances in magnetic memory technologies is the utilization of the giant spin Hall effect to switch a nanomagnet free layer in a magnetic tunnel junction (MTJ) structure. Due to the separate read and write channel, different aspects of the device can be engineered independently to satisfy different needs. We have shown that the reduction of Meff in the free layer can effectively reduce the switching current in the MTJs [1]. Another critical element of the MTJs is the spin Hall channel on which the switching voltage is applied where $V = I*R_{channel}$. In order to further reduce the V needed to operate these MTJs, we now design a shorter and narrower channel that can scale down the $R_{channel}$ significantly (Figure 1) with the accurate exposure from the ASML. This has enabled lower V_{c0} compared to previously reported for similar structures [2]. Excellent write error rate shows that these devices can be reliably used with infinite endurance, which is advantageous over other type of emerging memory technologies (Figure 2).

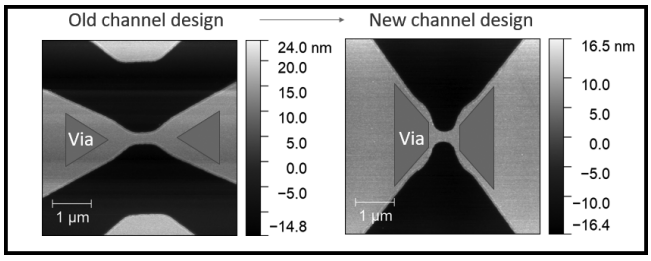

Figure 1: Schematic picture of the difference in the channel design.

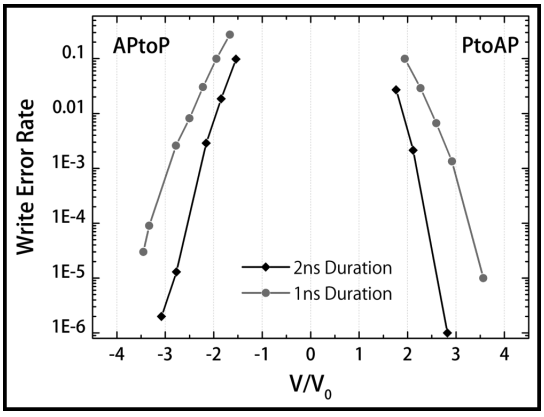

Figure 2: Write error rate measurement on a typical device made with the new mask design.

References:

[1] Shengjie Shi, Yongxi Ou, S. V. Aradhya, D. C. Ralph and R.A. Buhrman, Fast Low-Current Spin-Orbit-Torque Switching of Magnetic Tunnel Junctions through Atomic Modifications of the Free-Layer Interfaces. Phys. Rev. Applied. 9, 011002 (2018).

[2] Aradhya, S. V., Rowlands, G. E., Oh, J., Ralph, D. C., and Buhrman, R. A. Nanosecond-Timescale Low Energy Switching of In-Plane Magnetic Tunnel Junctions through Dynamic Oersted-Field-Assisted Spin Hall Effect. Nano Lett. 16, 5987-5992 (2016).

Spin Currents and Spin Fluctuations in Fe_xPt_{1-x} Alloys and Heterostructures

CNF Project Number: 111-80

Principal Investigator(s): Robert A. Buhrman

User(s): Ryan Tapping

Affiliation(s): Applied and Engineering Physics, Cornell University

Primary Source(s) of Research Funding: The Office of Naval Research, Cornell Center for Materials Research, National Science Foundation

Contact: buhrman@cornell.edu, rct76@cornell.edu

Primary CNF Tools Used: GCA 5x stepper, AJA sputtering tool

Abstract:

The spin Hall effect (SHE) is the conversion of a longitudinal charge current to a transverse spin current, often attributed to spin-orbit coupling. The magnetization of a thin film can be manipulated by spin-orbit torques (SOTs) generated by the SHE in an adjacent metallic layer, which has many promising applications in spintronics. Most research studying SOTs has focused on heavy metals such as Ta, Pt, and β-W, and more recently in alloys with other non-magnetic elements such as PtAu [1]. However, SOTs in systems with magnetic elements is not well understood. Recently it has been shown that the SOTs have a strong temperature dependence in Fe_xPt_{1-x} alloys [2]. The strength of the SHE in these ferromagnetic alloys, as measured through the damping-like spin torque efficiency, are enhanced near the Curie temperature, where there are strong spin fluctuations. We also look at the results of Fe/Pt multilayer heterostructures, where the strength of the magnetism can be adjusted by tuning the thicknesses of the ferromagnetic and heavy metal layers. Additionally, our work is continued to show that the Curie temperature can be tuned to be above room temperature, at working temperatures for possible computing applications.

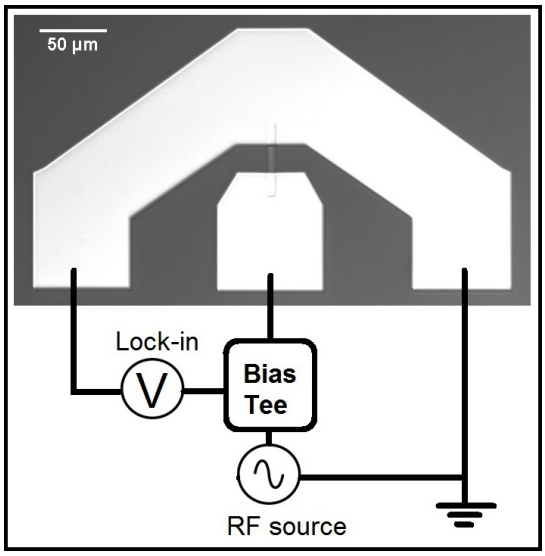

Figure 1: Microstrip after fabrication with top contacts and a schematic of the ST-FMR measurement.

Summary of Research:

Thin film samples were deposited onto 100 mm silicon wafers using our magnetron sputtering system. Structures were composed of, from bottom to top, Ta(1)/Fe_xPt_{1-x}(4)/FM(t)/MgO(2)/Ta(1) with numbers in parenthesis representing the thickness of the layer in nanometers and t, the thickness of the ferromagnetic layer (FM). Stacks were then patterned into 60 × 5 μm^2 microstrips using photolithography with the 5X g-line stepper at CNF and etched using our own ion milling system. The contacts were made using the AJA sputtering system at CNF.

Resistivity measurements, using a four probe method, showed that the FePt resistance increased with Fe concentration. Resistivities ranged from 40 µΩ.cm for pure Pt films to 88 and 101 µΩ.cm for Fe_xPt_{1-x} films with x = 0.23 and 0.35, respectively. This result is in agreement with previous reports and is indicative of the FM scattering impurities in the FePt [2]. Using Co as the FM layer, along with 0.4 nm of Pt spacer between the FePt and Co, the stacks have induced perpendicular magnetic anisotropy (PMA). When using FeCoB as the FM layer, the samples have in-plane anisotropy.

These two structures allow for different, independent measurements of the spin torque efficiency.

The spin torque efficiency (ξ) in the in-plane samples was determined using spin-torque ferromagnetic resonance (ST-FMR) [3]. This technique works by driving a microwave frequency (RF) current through the microstrip, which induces magnetic precession in the ferromagnetic layer via the spin transfer torque. A magnetic field is swept at 45° to the microstrip and the voltage is measured by a lock-in amplifier. A lineshape analysis is done by fitting a Lorentzian function with symmetric (S) and antisymmetric (A) components as shown in Figure 2. The ratio of the prefactors S and A yield ξ_{FMR}. By fitting $1/\xi_{FMR}$ vs 1/t, the damping-like (ξ_{DL}) and field-like (ξ_{FL}) spin torque efficiencies can be extrapolated.

Additionally PMA samples with cobalt as the FM layer were measured using an out-of-plane second harmonic technique [4]. Measurements of the resistance of the microstrips as an in-plane field is swept can yield information about the anisotropy field. Then second harmonic measurements of the resistance and fields are swept parallel and perpendicular to the applied current yield information about ξ_{DL} and ξ_{FL} through effective field determinations.

We observe that ξ_{DL} and ξ_{FL} are in the FePt alloys having a large temperature dependence, specifically near the Curie temperature (T_c). As shown in Figure 3 (published [2]), a large increase in the effective fields, H_{DL} and H_{FL} occurs near the ferromagnetic transition and the peak values are measured just above the Curie temperature, for two samples of different Fe concentration.

These results pave the way for future research and potential application of ferromagnetic systems with strong spin-orbit coupling and spin fluctuations.

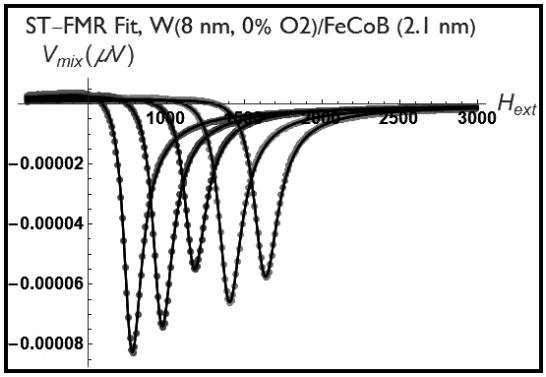

Figure 2: Example of voltage output from a magnetic field sweep from ST-FMR. Fits are also shown at 8, 9, 10, 11, and 12 GHz frequencies.

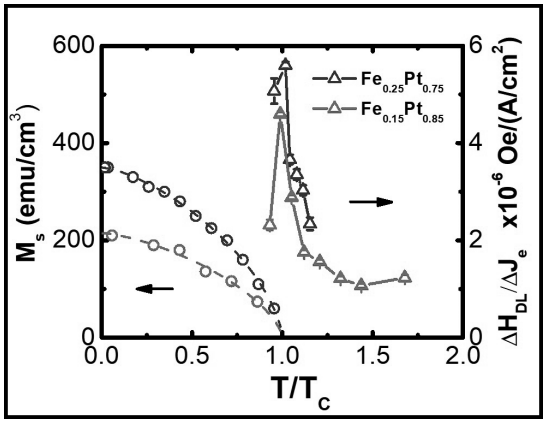

Figure 3: The temperature dependent magnetizations are plotted on the left for $Fe_{0.15}Pt_{0.85}$ and $Fe_{0.25}Pt_{0.75}$ samples, as a function of normalized temperature to the Curie temperature (T/T_c). Damping-like effective fields are plotted on the right as a function of normalized temperature, with a large enhancement observed near T_c.

References:

[1] L. Zhu, D.C. Ralph, and R.A. Buhrman, Phys. Rev. Applied 10, 031001 (2018).

[2] Y. Ou, D. C. Ralph, and R. A. Buhrman, Phys. Rev. Lett. 120, 097203 (2018).

[3] Chi-Feng Pai, Yongxi Ou, Luis Henrique Vilela-Leão, D.C. Ralph, and R.A. Buhrman, Phys. Rev. B. 92, 064426 (2015).

[4] M. Hayashi, J. Kim, M. Yamanouchi, and H. Ohno, Phys. Rev. B 89, 144425 (2014).

Non-Local Spin Transport in Complex Oxide Thin Films

CNF Project Number: 598-96

Principal Investigator(s): Daniel Ralph

User(s): Ruofan Li, Tianxiang Nan

Affiliation(s): Physics, Cornell University

Primary Source(s) of Research Funding: Army Research Office (W911NF-15-1-0447)

Contact: dcr14@cornell.edu, rl643@cornell.edu, tn272@cornell.edu

Primary CNF Tools Used: JEOL JBX-6300FS 100 kV electron-beam lithography system, scanning electron microscope, Veeco Icon atomic force microscope for high resolution profilometry

Abstract:

Magnon-mediated spin transport in magnetically-ordered insulators is of interest in the field of spintronics as it enables the transportation of spin information with ultra-low-dissipation compared with that by conduction electrons [1-4]. Recently, long-distance spin transport has been demonstrated in low-damping iron garnets, however the thicknesses of the iron garnet films that are required to possess low damping are typically over 100 nm. Efficient spin transport in low damping magnetic thin films with reduced thickness is essential for the integration of spintronic devices. In this work, we report long-distance spin transport in ultra-thin epitaxial films of magnesium aluminum ferrite ($MgAl_{0.5}Fe_{1.5}O_4$, MAFO). By exciting and detecting magnons by the spin Hall effect in Pt nanowires patterned on MAFO, we measured a magnon spin diffusion length of ~ 1 μm. This finding advances the study of magnon spin transport in the ultra-thin film regime.

Summary of Research:

MAFO is a newly-developed spinel ferrite material that can be grown in thin films [5]. High quality MAFO thin films possess a small Gilbert damping parameter (~0.0015) that is comparable to that of the well-known low-damping material yttrium iron garnet (YIG) but with a much thinner film thickness. This ultra-thin, low-loss and low-damping MAFO thin film could provide a good platform for the study of magnon transport and devices.

In this study, magnon transport is characterized in a non-local geometry (Figure 1b) in which two Pt nanowires are separated by a certain distance, with one nanowire acting as a spin injector and another one as a spin detector. Owing to the strong spin-Hall effect in Pt, current passing through the spin injector gives rise to the spin accumulation at the interface that can excite the magnons in MAFO depending on the relative orientation between the spin polarization and magnetization directions. Reciprocally, the magnons are detected non-locally as a voltage via the inverse spin-Hall effect in the neighboring nanowire.

Our thin films of MAFO were grown by pulsed laser deposition on $MgAl_2O_4$ <001> single crystal substrates in collaboration with the Yuri Suzuki group at Stanford. The nanowires were then defined using electron-beam lithography (JEOL 6300) and the subsequent deposition and lift-off of a 10 nm Pt thin film. The Pt films were deposited by DC magnetron sputtering in an argon atmosphere with a base pressure < 3×10^{-8} Torr. Finally, the metal contacts to the nanowires using Ti (5 nm)/Pt (100 nm) were patterned (JEOL 6300) and deposited (AJA sputtering system). The nanowire dimension is 200 nm wide and 10 um long with the wire separation ranging from 200 nm to 10 μm. In Figure 1a, we show a finished device.

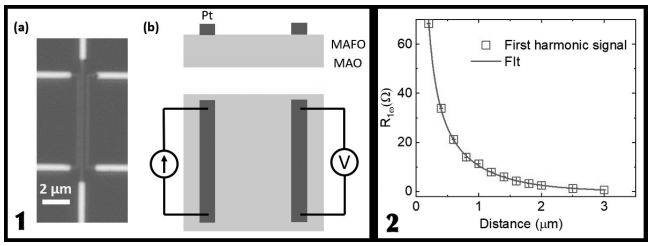

Figure 1, left: (a) Optical microscope image of a non-local Pt device on the MAFO thin film. (b) The device geometry and the measurement schematic.

Figure 2, right: The first-harmonic response of the non-local device as a function of the distance between the injector and the detector. The curve represents the fitting to a magnon diffusion model.

The non-local measurements were performed at room temperature in a magnetic probe station with an in-plane vector magnetic field. The non-local signal (both first and second-harmonic responses) was then measured as a function of angle φ between the nanowires and the in-plane magnetic field. A series of such nanowire pairs with different spacings between them were measured and their non-local resistances as a function of the separations are plotted as shown in Figure 2. Such decay of the non-local response can be well fitted to a magnon diffusion model [2]:

$$R = \frac{C}{\lambda} \frac{\exp(d/\lambda)}{1-\exp(d/\lambda)}$$

where C is a distance-independent constant, d is the injector-detector separation distance, and λ is the spin diffusion length of MAFO. The fitting gives a magnon spin diffusion length of 1 μm for a 10-nm-thick MAFO thin film.

In conclusion, we studied the magnon diffusion length in the ultra-thin magnetic insulator, MAFO films, using non-local measurements with Pt nanowire pairs.

Our observed decay of magnons over distance fits well with the spin diffusion model, from which the spin diffusion length in MAFO was extracted to be around 1 μm. This discovery demonstrates the potential of MAFO thin films as a new platform for energy-efficient spin transport.

References:

[1] Kajiwara, Y. et al. Transmission of electrical signals by spin-wave interconversion in a magnetic insulator. Nature 464, 262-266 (2010).

[2] Cornelissen, L. J., Liu, J., Duine, R. A., Youssef, J. Ben, and Van Wees, B. J. Long-distance transport of magnon spin information in a magnetic insulator at room temperature. Nat. Phys. 11, 1022-1026 (2015).

[3] Lebrun, R. et al. Tunable long-distance spin transport in a crystalline antiferromagnetic iron oxide. Nature 561, 222-225 (2018).

[4] Xing, W., Qiu, L., Wang, X., Yao, Y., and Ma, Y. Magnon Transport in Quasi-Two-Dimensional van der Waals Antiferromagnets. Phys. Rev. X 9, 11026 (2019).

[5] Emori, S. et al. Ultralow Damping in Nanometer-Thick Epitaxial Spinel Ferrite Thin Films. Nano Lett. 18, 4273-4278 (2018).

Photodiode Devices for Stimulation, Electrolysis, and Bubble Production

CNF Project Number: 900-00

Principal Investigator(s): Paul L. McEuen[1,2]

User(s): Samantha L. Norris[1], Michael F. Reynolds[1], Alejandro J. Cortese[1], Yanxin Ji[1]

Affiliation(s): 1. Laboratory of Atomic and Solid State Physics, Cornell University, Ithaca NY, USA; 2. Kavli Institute at Cornell for Nanoscale Science, Cornell University, Ithaca NY, USA

Primary Source(s) of Research Funding: Cornell Center for Materials Research with funding from the NSF MRSEC program (DMR-1719875), Air Force Office of Scientific Research (AFSOR) multidisciplinary research program of the university research initiative Grant FA2386-13-1-4118

Contact: plm23@cornell.edu, sn588@cornell.edu, mfr74@cornell.edu, ajc383@cornell.edu, yj323@cornell.edu

Primary CNF Tools Used: Oxford Cobra ICP etcher, ABM contact aligner, Oxford 100 etcher, Xactix XeF2 etcher, AJA sputter deposition Tool, Oxford PECVD

Abstract:

We present photodiode devices that can be fabricated and released from the substrate in massive parallel using traditional photolithographic techniques. In this report, we discuss fabrication and characterization of these devices, and show some proof of concept measurements for applications in neural stimulation, as well as electrophoretic motion and gas bubble production based on electrolysis.

Summary of Research:

The ability to locally produce voltages and currents with a microscale device that is optically powered lends itself well to a variety of applications. For instance, a cell-scale device would be minimally invasive when inserted into neural tissue and could electrically stimulate surrounding neurons. In addition, these devices can perform electrolysis of the surrounding water, locally changing the pH near the electrodes. Finally, during electrolysis the creation of oxygen and hydrogen gas at the electrodes causes bubble formation, the flow of which can be controlled by the geometry of the device itself.

The entire process utilizes silicon-on-insulator substrates and traditional photolithographic techniques, which enables the production of these devices and their release from the substrate to be performed in massive parallel. To create the silicon photodiode devices, we begin by selectively doping the top of the device layer with phosphosilicate glass to create a vertical PN junction. We then electrically isolate the photodiodes by dry etching to the underlying oxide layer in the Oxford Cobra inductively coupled plasma (ICP) etcher and connect them in series to apply voltages to two metal electrodes on either end of the device. The metal electrodes and interconnects are platinum with a titanium adhesion layer deposited in the AJA sputter deposition tool. We encapsulate the photodiodes with silicon dioxide with the Oxford plasma enhanced chemical vapor deposition tool, leaving the metal electrodes protruding. Finally, we release the devices into solution using a combination of dry and wet etches.

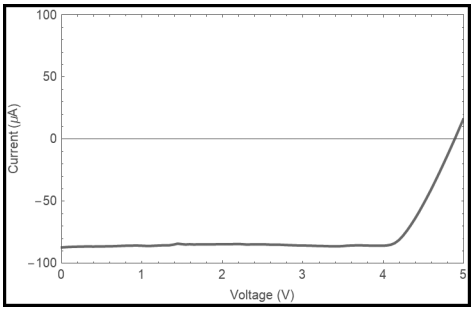

Figure 1: Current vs. bias voltage for a 100 μm, 7-PV photodiode device under 100 nW/μm², 532 nm laser illumination.

In the presence of incident light, a voltage proportional to the number of photovoltaics wired in series is applied between the electrodes. The current flowing through the device is proportional to the incident light intensity, allowing the electrical characteristics of the device to be tuned *in situ*. The current and voltage characteristics for a 100 μm, seven-photodiode device are shown in Figure 1. Such a device produces ~ 100 μA of current and ~ 4V. These values correspond to those typically used for microstimulation of neurons [1]. We are currently working on inserting these devices onto flight steering muscles in Drosophila melanogaster for in-flight stimulation.

When in solution, these devices perform electrolysis of the surrounding water, locally increasing or decreasing the pH near the anode and cathode,

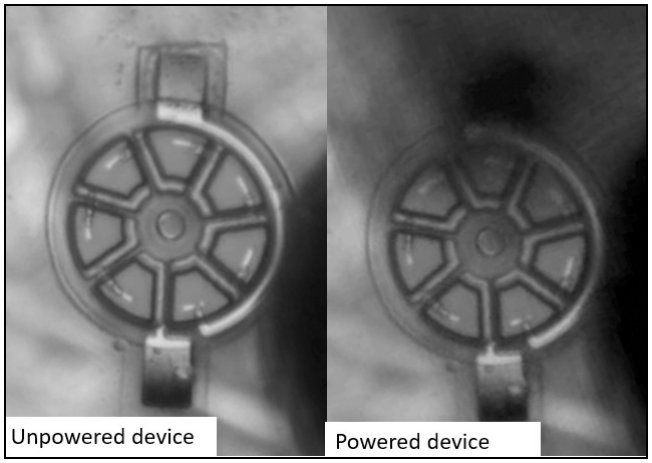

Figure 2: Unpowered and powered device in phenol red pH indicator dye. A darker color is indicative of a higher pH near the anode of the device.

respectively. Figure 2 shows a local pH change imaged by adding a colorimetric pH indicator dye, phenol red. These devices could be used as optically powered voltage sources for local electrochemistry or electrophoretic pumps in microfluidic environments and other enclosed geometries.

During electrolysis, the electrodes also drive the conversion of water to hydrogen and oxygen gas at the cathode and anode, respectively. The size and flow of these bubbles can be tuned by changing the geometry of the electrodes. Inspired by previous works on bubble rockets [2], we fabricated devices with a hollow cylinder-like electrode geometry that is tapered to allow bubbles to be preferentially ejected in one direction. Future work includes tuning device geometry to cause self-propulsion by bubble ejection and using bubble production in an enclosed space to cause devices to be neutrally buoyant.

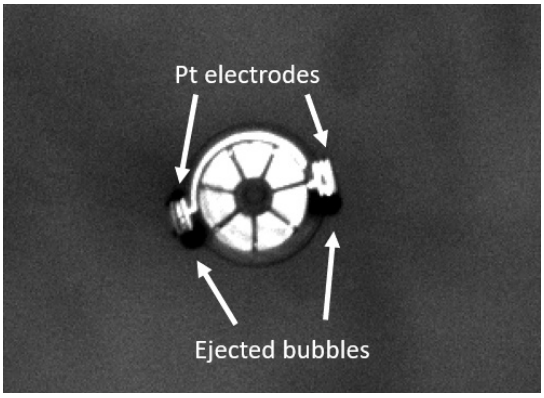

Figure 3: A typical photodiode device with tapered platinum electrodes for bubble production.

References:

[1] Ramasubbu, R. (2018). Dosing of Electrical Parameters in Deep Brain Stimulation (DBS) for Intractable Depression: A Review of Clinical Studies. Frontiers in Psychiatry.

[2] Gallino, G., Gallaire, F., Lauga, E., and Michelin, S. (2018). Physics of Bubble-Propelled Microrockets. Advanced Functional Materials.

Nanofabricated Superconducting Devices for Vortex Dynamics and Qubits

CNF Project Number: 1314-05

Principal Investigator(s): Britton L.T. Plourde

User(s): Kenneth Dodge, Jaseung Ku, Yebin Liu, Michael Senatore

Affiliation(s): Department of Physics, Syracuse University

Primary Source(s) of Research Funding: Army Research Office

Contact: bplourde@syr.edu, krdodgej@syr.edu, jku102@syr.edu, yliu166@syr.edu, masenato@syr.edu

Website: http://plourdelab.syr.edu

Primary CNF Tools Used: ASML photostepper, JEOL 9500, Plasma-Therm 770

Abstract:

We fabricate superconducting microwave devices for studying the dynamics of vortices at low temperatures and for forming novel qubits. Vortices are quantized bundles of magnetic flux that thread many different superconductors over a particular range of applied magnetic field. By using disordered superconducting thin films for high kinetic inductance wires, we are able to build structures that can lead to qubits that are protected against decoherence.

Summary of Research:

Superconducting microwave circuits play an important role in quantum information processing. Circuits composed of Josephson junctions and capacitors with superconducting electrodes can serve as qubits, the fundamental element of a quantum computing architecture. Various loss mechanisms limit the ultimate performance of these devices, including trapped magnetic flux vortices. Vortices can be trapped in the superconducting electrodes when background magnetic fields are present and contribute dissipation when driven with microwave currents [1]. Thus, techniques for controlling the trapping of vortices are critical to the development of large-scale quantum information processors with superconducting circuits. In addition, highly disordered superconducting films, including granular Al, can be used to form wires with a compact high kinetic inductance that can be combined with Al-AlO_x-Al Josephson junctions to form the central element for novel qubit designs that are protected against decoherence [2,3].

We fabricate our microwave resonators from various superconducting films, including aluminum, deposited onto silicon wafers in vacuum systems at Syracuse University. We define the patterns on the ASML stepper and transfer them into the films with a combination of reactive ion etching and liftoff processing. For defining Josephson junctions, we use the JEOL 9500 along with a dedicated deposition system at Syracuse University. We measure these circuits at temperatures of 100 mK and below in our lab at Syracuse University.

References:

[1] Song, C., Heitmann, T.W., DeFeo, M.P., Yu, K., McDermott, R., Neeley, M., Martinis, John M., Plourde, B.L.T.; "Microwave response of vortices in superconducting thin films of Re and Al"; Physical Review B 79, 174512 (2009).

[2] Doucot, B., Ioffe, L.; "Physical implementation of protected qubits"; Reports on Progress in Physics 75, 072001 (2012).

[3] Liu, Y., Dodge, K., Senatore, M., Zhu, S., Naveen, Shearrow, A., Schlenker, F., Klots, A., Faoro, L., Ioffe, L., McDermott, R., Plourde, B.; "Implementation of pi-periodic Josephson Elements for Topologically Protected Charge-Parity Qubits"; Bull. Am. Phys. Soc. 2019, http://meetings.aps.org/Meeting/MAR19/Session/S26.11.

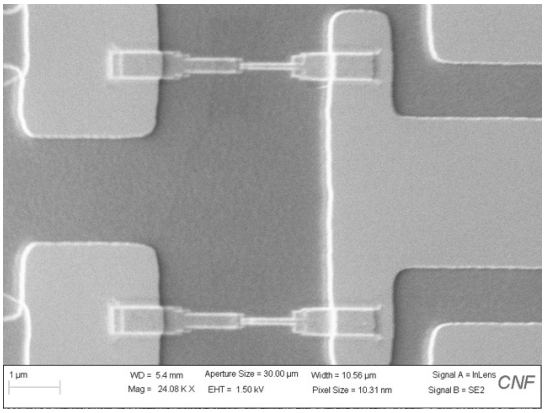

Figure 1: Scanning electron micrograph of Al-AlO_x-Al Josephson junctions in protected qubit design.

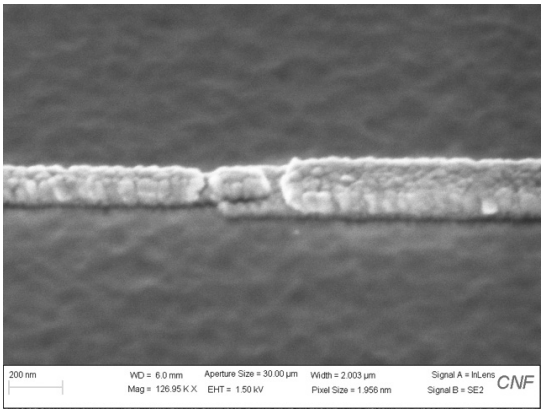

Figure 2: Scanning electron micrograph closeup image of Al-AlO_x-Al Josephson junction on protected qubit element.

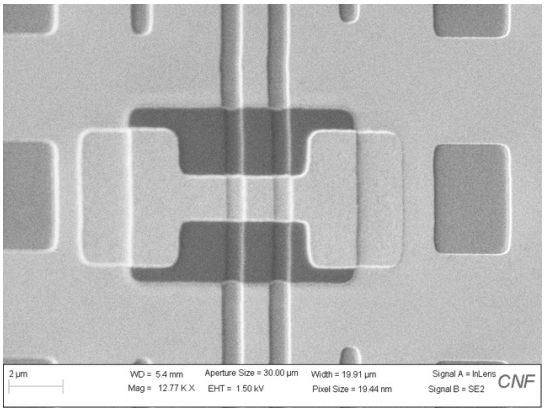

Figure 3: Scanning electron micrograph of Nb ground connection over SiO_x spacer on protected qubit element.

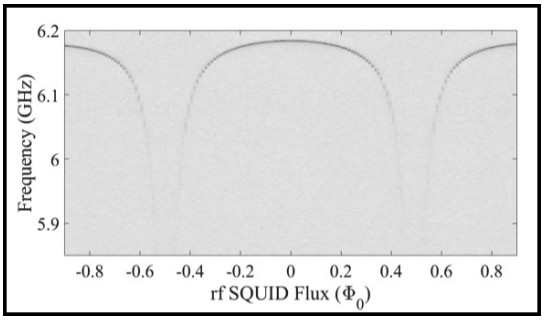

Figure 4: Measurement of magnetic flux modulation of microwave resonance from protected qubit element.

Fabrication of Nanofluidic Cavities for Superfluid ^{3}He Studies

CNF Project Number: 1520-07

Principal Investigator(s): Jeevak M. Parpia

User(s): Abhilash Thanniyil Sebastian, Nikolay Zhelev

Affiliation(s): Department of Physics, Cornell University

Primary Source(s) of Research Funding: National Science Foundation

Contact: jmp9@cornell.edu, nizhelev@gmail.com, abhilashthanniyil@gmail.com

Website: http://parpia.lassp.cornell.edu

Primary CNF Tools Used: Oxide furnace, Oxford PECVD, Oxford and Plasma-Therm RIE, dicing saw

Abstract:

We demonstrate nanoscale cavities that withstand 30 bar cooled to ultralow temperatures [1]. These structures have been utilized to observe an unexpected spatially modulated order parameter in superfluid ^{3}He [2].

Summary of Research:

Superfluid ^{3}He is a unique system for study. ^{3}He is a Fermion (like electrons), but its pairing into the superfluid state is more complex than its electronic counterparts producing a multiplicity of superfluid phases. In the bulk the anisotropic A phase and the isotropically gapped B phase emerge. Confinement favors the A phase over the B phase [2,3,4].

The superfluid state is attained between 0 and 35 bar and between 0.9 and 2.5 mK (respectively). Below the superfluid transition, pairs condense into the coherent superfluid state. The pairing length-scale (pair diameter) varies from ~ 80 nm at 0 bar to 14 nm at high pressure. Confinement alters the phase diagram and as the ^{3}He is progressively restricted to smaller sizes, the B phase should yield to the A phase and new phases should emerge.

A recent experiment [2], carried out by colleagues at Royal Holloway in London, explored the magnetic signatures of ^{3}He confined in a 1.1 μm tall chamber. Extracting signals from the ~ 70 nL sample at temperatures well below 1 mK required using their highly sensitive SQUID NMR techniques.

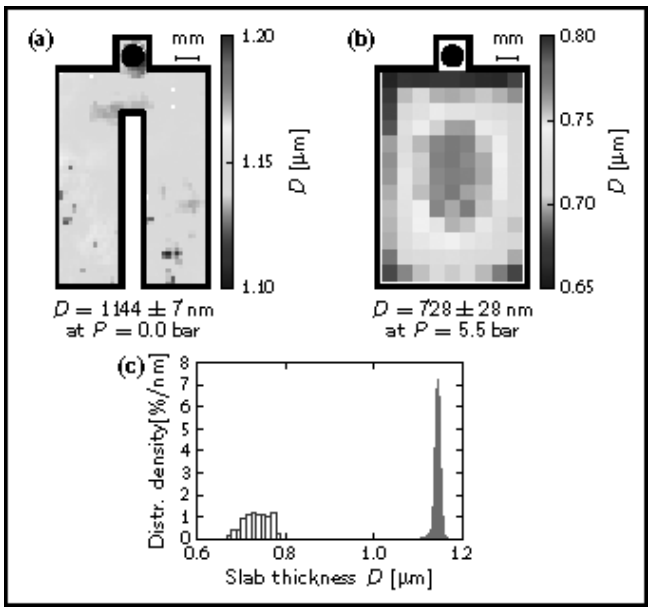

Figure 1: (a) Comparison of the heights within the new cell used in experiment [2] compared to (b) previous generation cell (at 5.5 bar pressure) using 3 mm thick silicon and glass. The addition of a "septum" to reduce the unsupported span results in a much more uniform spacing. The cavity dimensions are approximately 7 mm × 11 mm. (c) shows a comparison in height distributions of the two cells, the right one being the data from the newer cell, and the broader distribution at left, showing the height distribution measurement for the older cell.

To fabricate this device, a 1 mm thick silicon wafer was oxidized using the oxide furnace in CNF to grow thick oxide (> 2 μm), then further oxide was deposited using the Oxford PECVD. The device was patterned using contact photolithography and the oxide removed using both dry plasma etch (Oxford and Plasma-Therm RIE) and wet etch (6:1 BOE). The wafer was further oxidized to create a step in the Si-SiO_2 interface (modified LOCOS process) and oxide removed using HF. The chips were then diced using CNF's dicing saw. Matching polished glass pieces were also diced.

The final step to make the cells was to remove oxide off Si pieces, clean in SC-1 solution and bond using custom made anodic bonding jig. The resulting bonded cell had a very uniform height distribution (Figure 1 a, c) in comparison to previous cells (Figure 1 b).

The experiments represent the melding of theory (experiments were initiated following a seminal theory result [5] that predicted stripes), the development of fabrication and sealing technology over several years [1], and a whole suite of experimental measurement techniques [2,3,4]. The final results that point to a "polka dot configuration" rather than the simpler proposed striped configuration have received wide publicity [6].

Former Physics Ph.D. students Nikolay Zhelev (now Corning Research), Roberto DeAlba (now INTEL), and post-doctoral scientist Abhilash Sebastian (now VTT Research Labs, Finland) fabricated these structures before they left Cornell. Results from these structures are now emerging or have been recently published.

References:

[1] Fabrication of microfluidic cavities using Si-to-glass anodic bonding; N. Zhelev, T. S. Abhilash, R. G. Bennett, E. N. Smith, B. Ilic, L. V. Levitin, X. Rojas, A. Casey, J. Saunders, and J. M. Parpia, Rev. Sci. Instr., 073902-1-10, 89, https://doi.org/10.1063/1.5031837 (2018).

[2] Evidence for a Spatially Modulated Superfluid Phase of ^{3}He under Confinement; Lev V. Levitin, Ben Yager, Laura Sumner, Brian Cowan, Andrew J. Casey, John Saunders, Nikolay Zhelev, Robert G. Bennett, and Jeevak M. Parpia, Phys. Rev. Lett. 122, 085301, https://journals.aps.org/prl/abstract/10.1103/PhysRevLett.122.085301 (2019).

[3] Phase Diagram of the Topological Superfluid ^{3}He Confined in a Nanoscale Slab Geometry; L. V. Levitin, R. G. Bennett, A. Casey, B. Cowan, J. Saunders, D. Drung, Th. Schurig and J. M. Parpia, Science, 340 841-844, https://science.sciencemag.org/content/340/6134/841 (2013).

[4] The A-B transition in superfluid helium-3 under confinement in a thin slab geometry; N. Zhelev, T.S. Abhilash, E.N. Smith, R.G. Bennett, X. Rojas, L. Levitin, J. Saunders, and J.M. Parpia, Nature Comm. 8 15963, https://www.nature.com/articles/ncomms15963 (2017).

[5] Crystalline order in superfluid ^{3}He Films; J. A. Sauls, and A. B. Vorontsov, Phys.Rev. Lett.98, 045301, https://journals.aps.org/prl/abstract/10.1103/PhysRevLett.98.045301 (2007).

[6] Viewpoint: A Polka-Dot Pattern Emerges in Superfluid Helium, Jochen Wosnitza, Physics 12, 20, https://physics.aps.org/articles/v12/20, February 27, 2019.

Fabrication of Nanoscale Josephson Junctions for Quantum Coherent Superconducting Circuits

CNF Project Number: 1735-08

Principal Investigator(s): Britton L.T. Plourde

User(s): Andrew Ballard, Caleb Howington, Indrajeet

Affiliation(s): Department of Physics, Syracuse University

Primary Source(s) of Research Funding: Army Research Office, National Science Foundation

Contact: bplourde@syr.edu, alballar@syr.edu, cjhowing@syr.edu, indraje@syr.edu

Website: http://plourdelab.syr.edu

Primary CNF Tools Used: ASML stepper, JEOL 9500, Plasma-Therm 770

Abstract:

We fabricate nanoscale superconductor tunnel junctions and other structures for experiments involving quantum coherent circuits. Such circuits have shown great promise in recent years for explorations of quantum mechanics at the scale of circuits on a chip and for forming qubits, the foundational elements of a quantum computer. The quantum state of these superconducting qubits can be manipulated with microwave radiation at low temperatures. In addition, we are developing alternative techniques for probing the state of these qubits and controlling their quantum state using superconducting digital circuitry, as well as superconducting metamaterial structures with novel microwave mode spectra for coupling to superconducting qubits.

Summary of Research:

The unique properties of nanoscale Josephson junctions enable a wide range of novel superconducting circuits for investigations in many diverse areas. In recent years, circuits composed of such junctions have emerged as promising candidates for the element of a quantum computer, due to the low intrinsic dissipation from the superconducting electrodes and the possibility of scaling to many such qubits on a chip [1]. The quantum coherent properties of the circuits are measured at temperatures below 50 mK with manipulation of the qubit state through microwave excitation.

We are currently working on a variety of experiments involving these nanoscale Josephson junctions and other superconducting structures that allow us to probe novel quantum effects in our microwave circuits. We are fabricating superconducting circuits for forming low-temperature detectors of single microwave photons and for implementing a new scheme for the efficient readout of the quantum state of superconducting qubits [2,3]. We are also working with collaborators at the University of Wisconsin, Madison to develop hybrid quantum/classical superconducting chips that allow us to perform coherent quantum control of a superconducting qubit based on digital pulses from a Single Flux Quantum (SFQ) circuit [4,5].

In another effort, we are using particular combinations of superconducting lumped-circuit elements to engineer metamaterial transmission lines that exhibit novel mode structures characteristic of left-handed materials. We are fabricating such metamaterial transmission lines from Al and Nb films on Si and characterizing these at low temperatures [6]. We are working on experiments to couple these left-handed lines to superconducting qubits for experiments involving the exchange of microwave photons [7].

We pattern these circuits at the CNF with nanoscale structures defined with electron-beam lithography on the JEOL 9500 integrated with photolithographically defined large-scale features. The junctions are fabricated using the standard double-angle shadow evaporation technique, in which a resist bilayer of copolymer and PMMA is used to produce a narrow PMMA airbridge suspended above the substrate. Evaporation of aluminum (Al) from two different angles with an oxidation step in between forms a small Al-AlO_x-Al tunnel junction from the deposition shadow of the airbridge. We have developed a process for defining these junctions with electron-beam lithography and we perform the aluminum evaporations in a dedicated chamber at Syracuse.

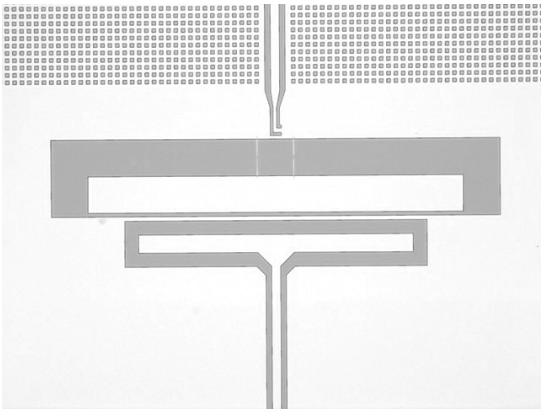

Figure 1: Optical micrograph of superconducting qubit for digital control experiments.

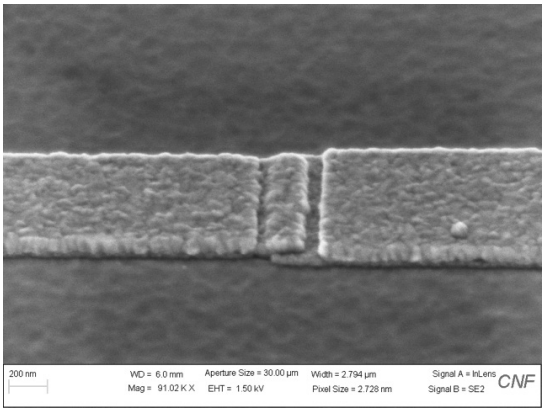

Figure 2: Scanning electron micrograph of Al-AlO_x-Al Josephson junction for superconducting qubit.

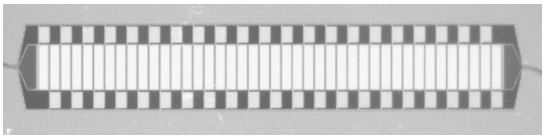

Figure 3: Optical micrograph of superconducting metamaterial transmission line resonator fabricated from Nb thin film on Si.

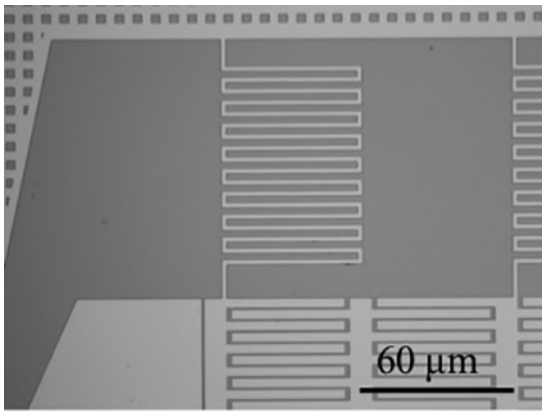

Figure 4: Optical micrograph of meander-line inductor and portion of interdigitated capacitor on metamaterial transmission line resonator fabricated from Nb thin film on Si.

We pattern large-scale features using the ASML stepper, with electron-beam evaporation of Al, sputter-deposition of Nb, and PECVD deposition of SiO_2.

Measurements of these circuits are performed in cryogenic systems at Syracuse University, including dilution refrigerators for achieving temperatures below 30 mK.

References:

[1] Clarke, J. and Wilhelm, F.K.; "Superconducting quantum bits"; Nature, 453, 1031 (2008).

[2] Govia, L.C.G., Pritchett, Emily J., Xu, Canran, Plourde, B. L. T., Vavilov, Maxim G., Wilhelm, Frank K., McDermott, R.; "High-fidelity qubit measurement with a microwave-photon counter"; Physical Review A 90, 062307 (2014).

[3] Opremcak, A, Pechenezhskiy, I., Howington, C., Christensen, B.G., Beck, M.A., Leonard Jr, E., Suttle, J., Wilen, C., Nesterov, K.N., Ribeill, G.J., Thorbeck, T., Schlenker, F., Vavilov, M.G., Plourde, B.L.T., McDermott, R.; "Measurement of a Superconducting Qubit with a Microwave Photon Counter"; Science 361, 1239 (2018).

[4] McDermott, R., Vavilov, M.; "Accurate Qubit Control with Single Flux Quantum Pulses"; Physical Review Applied 2, 014007 (2014).

[5] Leonard, E., Beck, M., Nelson, JJ, Christensen, B., Thorbeck, T., Howington, C., Opremcak, A.,Pechenezhskiy, I., Dodge, K., Dupuis, N., Ku, J., Schlenker, F., Suttle, J. Wilen, C., Zhu, S., Vavilov, M., Plourde, B, McDermott, R.. "Digital coherent control of a superconducting qubit"; Physical Review Applied 11, 014009 (2019).

[6] Wang, H., Zhuravel, A., Indrajeet, S., Taketani, B., Hutchings, M., Hao, Y., Rouxinol, F., Wilhelm, F., LaHaye, M.D., Ustinov, A., Plourde, B.; "Mode Structure in Superconducting Metamaterial Transmission Line Resonators"; Physical Review Applied 11, 054062 (2019).

[7] Indrajeet, S., Wang, H., Hutchings, M., LaHaye, M., Taketani, Bruno, Wilhelm, F., Plourde, B.; "Qubit Dynamics in a Multi-mode Environment with a Superconducting Metamaterial Resonator"; Bull. Am. Phys. Soc. 2019, http://meetings.aps.org/Meeting/MAR19/Session/P26.4.

Spin Seebeck Imaging of Spin-Torque Switching in Antiferromagnetic Pt/NiO Heterostructures

CNF Project Number: 2091-11

Principal Investigator(s): Gregory D. Fuchs[1]

User(s): Isaiah Gray[1], Gregory M. Stiehl[2]

Affiliation(s): 1. School of Applied and Engineering Physics, Cornell University, Ithaca, NY 14853; 2. Department of Physics, Cornell University, Ithaca, NY 14853

Primary Source(s) of Research Funding: Cornell Center for Materials Research from the National Science Foundation MRSEC Program, Grant No. DMR-1719875

Contact: gdf9@cornell.edu, ig246@cornell.edu, gms263@cornell.edu

Primary CNF Tools Used: GCA 5x stepper

Abstract:

As electrical control of Néel order opens the door to reliable antiferromagnetic (AF) spintronic devices, understanding the microscopic mechanisms of AF switching is crucial. Spatially-resolved studies are necessary to distinguish multiple nonuniform switching mechanisms; however, progress has been hindered by the lack of tabletop techniques to image the Néel order. We demonstrate spin Seebeck microscopy as a sensitive table-top method for imaging antiferromagnetic order in thin films and apply this technique to study spin-torque switching in NiO/Pt and Pt/NiO/Pt heterostructures. We establish the interfacial antiferromagnetic spin Seebeck effect in NiO as a probe of surface Néel order. By imaging before and after applying current-induced spin torque, we resolve spin domain rotation and domain wall motion, acting simultaneously.

Summary of Research:

Antiferromagnets (AFs) are attractive candidates for spintronic devices due to their lack of stray fields, their terahertz switching speeds, and their stability to magnetic field [1]. They are also notoriously difficult to read and write [2]. Recent demonstrations of electrical switching of Néel order [3-6] may provide a path to overcome this difficulty and potentially construct practical devices. However, AF switching is nonuniform and multiple switching mechanisms contribute simultaneously, making device-level readout difficult to interpret. Systematic imaging studies of AF switching are necessary to understand the microscopic mechanisms. The best-established technique for imaging Néel order — XMLD-PEEM7 — requires synchrotron facilities that are generally only available in 24-48-hour runs, therefore tabletop imaging techniques are necessary to better understand and optimize AF switching.

In this work [8] we demonstrate spin Seebeck microscopy as a sensitive tabletop probe of the Néel order and image current-induced spin-torque switching in antiferromagnetic Pt/NiO and Pt/NiO/Pt heterostructures.

Our technique is based on the interfacial antiferromagnetic longitudinal spin Seebeck effect (AF-LSSE) [9] in so-called *uncompensated* antiferromagnets such as the insulator NiO<111>, in which the spins in the interfacial layer are aligned parallel as shown schematically in Figure 1(a). A local thermal gradient at this interface generates a spin current that reports the Néel orientation of the interfacial spins. We generate local thermal gradients by focusing a pulsed laser to 650 nm spot size and detect the resulting spin current by transducing it into a charge current through the inverse spin Hall effect in the adjacent Pt layer. We therefore measure the in-plane component of the surface Néel orientation. Figure 1(b) shows an example AF LSSE image of a 20 μm-wide Hall bar of 165 nm NiO<111>/ Pt on $MgAl_2O_4$. Blue and red $V_{AF\ LSSE}$ contrast represents spins pointing towards the right and left, respectively.

In contrast to an uncompensated AF, Figure 1(c) diagrams a *compensated* AF, in which the spins in the interfacial layer are anti-aligned. The spin current from this interface should cancel out to zero over the laser spot area. To test this prediction, in Figure 1(d) we image

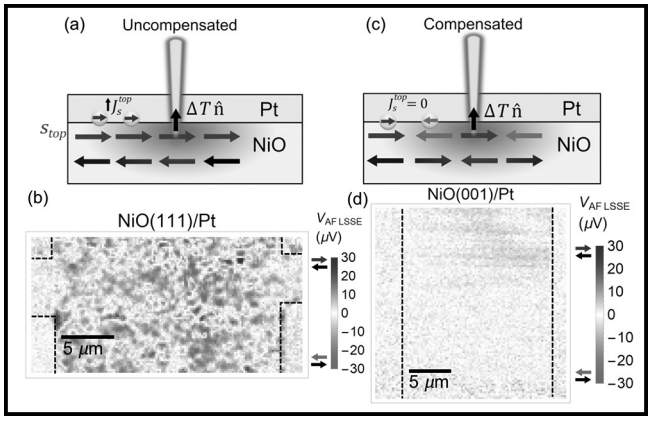

Figure 1: Demonstrating interfacial antiferromagnetic longitudinal spin Seebeck effect (AF LSSE). (a) Diagram of uncompensated NiO<111>/Pt, in which the spins on the top interface are aligned. A thermal gradient across this interface generates a spin current that reports the surface Néel orientation. (b) AF LSSE image of a 165 nm NiO<111>/Pt sample, showing AF domains. (c) Diagram of compensated NiO<001>/Pt, in which the spins on the top interface are anti-aligned and produce no net spin current. (d) AF LSSE image of a 136 nm NiO<001>/Pt sample, showing no measurable contrast. (Find full color on pages xiv-xv.)

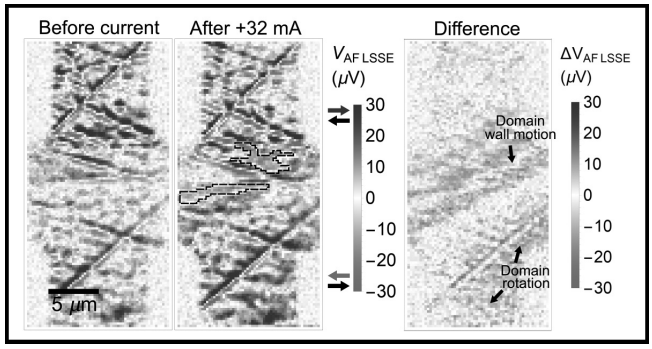

Figure 2: AF LSSE images of Pt/6 nm NiO<111> before and after applying 7 × 10⁷A/cm² DC current. Prominent regions of switching are highlighted. The difference image shows switching both by rotation of AF domains and by domain wall motion. (Find full color on pages xiv-xv.)

another 20 μm-wide Hall bar of 136 nm NiO<001>/Pt on MgO<001>, similar to the NiO<111>/Pt sample except that NiO<001> has a compensated interface. We obtain no measurable contrast from NiO<001> compared with NiO<111>, which confirms that the uncompensated interface is necessary and indicates that we indeed measure surface Néel order.

We then image spin-torque switching in a 10 μm-wide device of Pt/6 nm NiO<111> in Figure 2. We image before and after applying 7 × 10^7A/cm^2 current density along the device and take the difference to show the changes in domain structure. Prominent regions of switching are highlighted in black dashed line. The lower portion of the difference image shows nearly uniform contrast, meaning different AF domains rotate by the same angle. The middle of the channel shows adjacent regions of blue and red, which indicate domain wall motion in response to current. Our findings are consistent with recently-developed models of spin-torque switching in NiO/Pt[6].

In conclusion, we demonstrate spin Seebeck microscopy as a powerful tabletop technique for imaging surface Néel order in an antiferromagnetic insulator and apply this technique to image spin-torque switching in NiO/Pt heterostructures. We find that switching occurs by domain rotation and domain wall motion acting simultaneously. Our results provide critical insight into the complex processes in electrical control of antiferromagnetism and we expect our technique to generalize to a variety of antiferromagnetic insulators.

References:

[1] T. Jungwirth, et al., Nat. Nano. 11, 231-241 (2016).
[2] C. Song, et al., Nanotechnology 29, 112001 (2018).
[3] P. Wadley, et al., Science 351, 587-590 (2016).
[4] T. Moriyama, et al., Scientific Reports 8, 14167 (2018).
[5] X. Z. Chen, et al., Phys. Rev. Lett. 120, 207204 (2018).
[6] L. Baldrati, et al., arXiv:1810.11326 (2018).
[7] J. Stöhr, et al., Phys. Rev. Lett. 83, 1862 (1999).
[8] I. Gray, et al., arXiv:1810.03997 (2018).
[9] S. A. Bender, et al., Phys. Rev. Lett. 119, 056804 (2017).

Fabrication and Measurements of Arrays of Constriction-Based Spin-Hall Nano-Oscillators

CNF Project Number: 2091-11

Principal Investigator(s): Gregory D. Fuchs

User(s): Yanyou Xie

Affiliation(s): Applied and Engineering Physics, Cornell University

Primary Source(s) of Research Funding: National Science Foundation

Contact: gdf9@cornell.edu, yx322@cornell.edu

Primary CNF Tools Used: JEOL 9500, MA6 contact aligner

Abstract:

Spin-Hall nano-oscillators (SHNOs) convert D.C. charge current to microwave frequency magnetic oscillations — enabling applications as highly agile microwave sources. The use of SHNOs for applications is still limited by the output microwave power and linewidth. The goal of this project is to synchronize SHNOs to generate larger power and narrower spectral linewidth. We are currently working on making arrays of SHNOs of different geometries and studying how they synchronize.

Summary of Research:

A spin-Hall nano-oscillator (SHNO) is a bilayer system containing a ferromagnetic layer and a metal layer with strong spin-orbit coupling [1], patterned as a nanowire or a nanoconstriction. SHNOs are based on spin-Hall effect, which converts a lateral charge current in the metal layer into a transverse pure spin current [2]. The spin current can provide sufficiently large spin transfer torque (STT) to the adjacent ferromagnetic layer to compensate the local spin wave damping, leading to auto-oscillations of the magnetic moment in the microwave regime [2]. For microwave oscillators, it is desirable to generate a larger power and a narrower spectral linewidth [3]. Arrays of synchronized SHNOs can reach these goals and the fabrication of arrays of constriction-based SHNOs is practical [1,3]. Here we fabricated arrays of two and four constriction-based SHNOs on 20.5 μm × 4 μm wires, with constriction width of 100 nm and 150 nm.

The fabrication process consists of three stages — sputtering, e-beam lithography and photolithography — as shown in Figure 1. We started by sputtering a bilayer of $Pt_{0.75}Au_{0.25}$ (5 nm)/$Ni_{81}Fe_{19}$ (5 nm) on a 2-inch sapphire wafer. Next, the SHNO devices were fabricated using e-beam lithography in JEOL 9500 to define constrictions with a 100 nm or 150 nm characteristic dimension. The SEM and AFM images of selected fabricated devices are shown in Figure 2 and 3. Finally, we fabricated gold bonding pads by photolithography. The process used the positive photoresist S1813 in the MA6 contact aligner. After developing, the we evaporated Cr (10 nm)/Au (90 nm) and performed lift-off.

Figure 4 shows spin-torque ferromagnetic resonance (ST-FMR) [4] measurements on one of the 4-constriction devices. In a ST-FMR measurement, a microwave-frequency (rf) charge current is applied to the SHNO, generating an oscillating transverse spin current and thus oscillating STT [4]. The oscillating STT induces magnetization precession in $Ni_{81}Fe_{19}$, which results in an oscillating resistance due to the anisotropic magnetoresistance of $Ni_{81}Fe_{19}$ [4]. Here we measure the generated D.C. differential voltage from the mixing of the rf current and the oscillating resistance [4], dV_{mix}/dH, as we sweep the external magnetic field. The occurrence of valley and peak (dark and light) combination indicates resonant excitation of spin wave eigenmodes [5]. Two significant valley and peak combination can be identified in Figure 4. By comparing with literature [5,6], we identified that at the same external magnetic field, the ones occurring at lower frequency are edge spin-wave modes, while the ones occurring at higher frequency are bulk spin-wave modes. The magnetization of the former mainly occurs near the edge of wire, while that of the latter mainly occurs in the interior of the wire [6]. To extract the mode profiles, we still need to perform micromagnetic simulations at the peak frequencies.

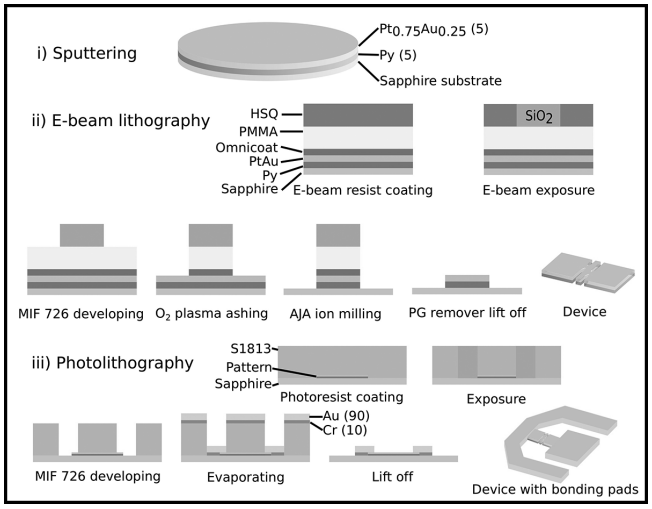

Figure 1: Fabrication process flow. (Find full color on pages xiv-xv.)

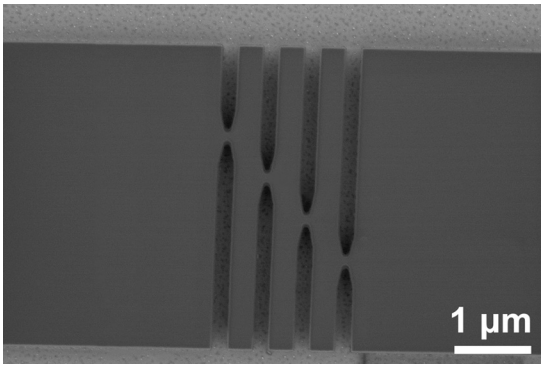

Figure 2: SEM image of one of the devices.

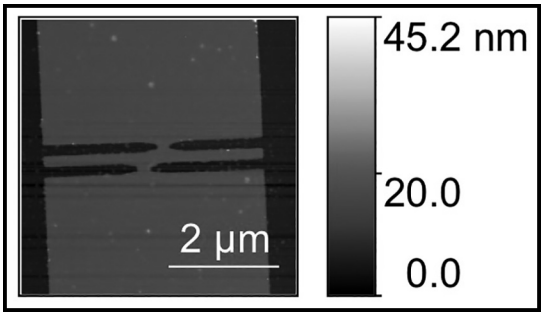

Figure 3: AFM image of one of the devices.

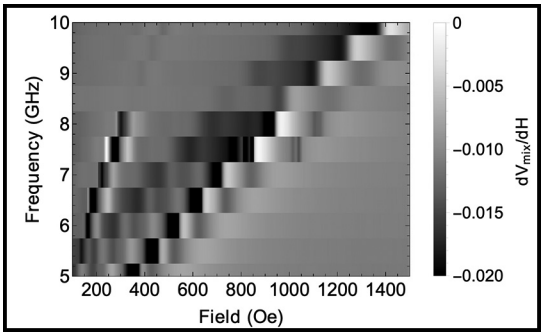

Figure 4: Density plot of spin-torque ferromagnetic resonance measurements sweeping along the external magnetic field. (Find full color on pages xiv-xv.)

References:

[1] Kendziorczyk, T., and T. Kuhn. "Mutual synchronization of nanoconstriction-based spin Hall nano-oscillators through evanescent and propagating spin waves." Physical Review B 93, no. 13 (2016): 134413.

[2] Dürrenfeld, Philipp, Ahmad A. Awad, Afshin Houshang, Randy K. Dumas, and Johan Åkerman. "A 20 nm spin Hall nano-oscillator." Nanoscale 9, no. 3 (2017): 1285-1291.

[3] Demidov, V. E., S. Urazhdin, A. Zholud, A. V. Sadovnikov, and S. O. Demokritov. "Nanoconstriction-based spin-Hall nano-oscillator." Applied Physics Letters 105, no. 17 (2014): 172410.

[4] Liu, Luqiao, Takahiro Moriyama, D. C. Ralph, and R. A. Buhrman. "Spin-torque ferromagnetic resonance induced by the spin Hall effect." Physical review letters 106, no. 3 (2011): 036601.

[5] Duan, Zheng, Andrew Smith, Liu Yang, Brian Youngblood, Jürgen Lindner, Vladislav E. Demidov, Sergej O. Demokritov, and Ilya N. Krivorotov. "Nanowire spin torque oscillator driven by spin orbit torques." Nature communications 5 (2014): 5616.

[6] Duan, Zheng, Carl T. Boone, Xiao Cheng, Ilya N. Krivorotov, Nathalie Reckers, Sven Stienen, Michael Farle, and Jürgen Lindner. "Spin-wave modes in permalloy/platinum wires and tuning of the mode damping by spin Hall current." Physical Review B 90, no. 2 (2014): 024427.

Diamond and SiC Semi-Confocal Acoustic Resonator

CNF Project Number: 2126-12

Principal Investigator(s): Gregory D. Fuchs[1]

User(s): Huiyao Chen[2]

Affiliation(s): 1. School of Applied and Engineering Physics, 2. Department of Physics; Cornell University

Primary Source(s) of Research Funding: Office of Naval Research (Grants No. N000141410812 and No. N000141712290)

Contact: gdf9@cornell.edu, hc846@cornell.edu

Website: http://fuchs.research.engineering.cornell.edu

Primary CNF Tools Used: PT770 etcher, GCA 5x stepper, Heidelberg mask writer DWL2000, AJA sputtering deposition system, odd/even evaporator, YES Asher, P10 profilometer, Westbond 7400A ultrasonic wire bonder

Abstract:

We report the design and fabrication of a semi-confocal high-overtone bulk acoustic resonator (SCHBAR) device on diamond (silicon carbide) with $f \cdot Q > 10^{12}$ ($> 10^{13}$) [1]. The semi-confocal geometry confines the phonon mode laterally below 10 µm. The device also has integrated atomic-scale quantum defects, and is thus suitable for quantum control applications such as mechanical manipulation of the defect spin states.

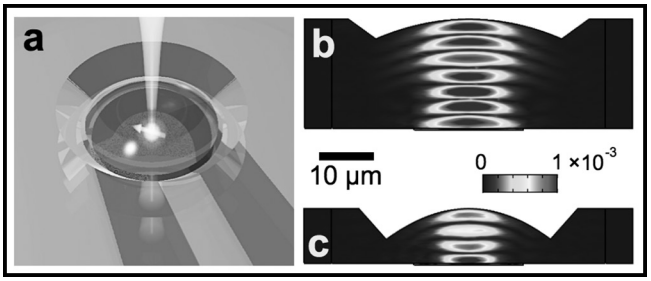

Figure 1: (a) Concept image of the semi-confocal HBAR device design. (b) and (c) are strain profiles of the diamond devices simulated by COMSOL for a 3 GHz mode, with a 1 V_p voltage driving source.

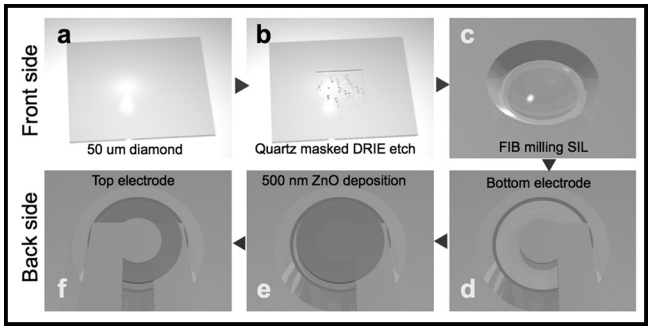

Figure 2: Fabrication process flow of the device starting from (a) a 50-µm-thick double- side-polished diamond plate; (b) DRIE etch a diamond membrane down to 20 µm or 10 µm using Ar/Cl_2 and O_2 plasma, using a laser cut quartz mask; (c) Mill the parabolic SIL using focused Ga ion beam. (d-f) A ZnO piezoelectric transducer is fabricated on the backside of the SIL.

Summary of Research:

As illustrated in Figure 1, the device has a planar-convex structure. We design one side of the resonator with a curved surface, enabling it to confine three dimensional phonon modes with characteristic dimensions of 10 µm. The radius of curvature of the curved surface is twice the thickness of the substrate in a semi-confocal geometry, giving rise to the device name, SCHBAR.

Compared to a planar cavity, the curved surface eliminates the requirement of boundary parallelism and, in principle, yields higher mechanical quality factors. Optically, the curved surface also acts as a solid immersion lens (SIL) [2]. It reduces substrate refraction and thus enhances light extraction from the defects inside the resonator. The defects are microns below the surface and thus are well-protected from fabrication damage and surface effects. On the planar side of the device, we fabricate an integrated piezoelectric transducer and a microwave antenna that is aligned with the center of the resonator, allowing for acoustic and magnetic driving, respectively. The radius of the transducer has been designed to mode-match the waist of the confined acoustic wave, and the thickness of piezoelectric ZnO film is controlled to target a 3 GHz resonance mode, which allows stable confinement.

We fabricated SCHBAR devices from both diamond and 4H-SiC substrates. For simplicity, we restricted the process flow description to diamond (Figure 2). We start from a 50-µm-thick, double-side polished single crystal diamond plate (nitrogen concentration < 1 ppm). In the first step, we etch 5 µm of diamond on each side of the substrate using Ar/Cl_2 [3] and O_2 [4] plasma as a stress-relief etch to eliminate the residual polishing damage. A laser-cut quartz shadow mask is then used to mask the

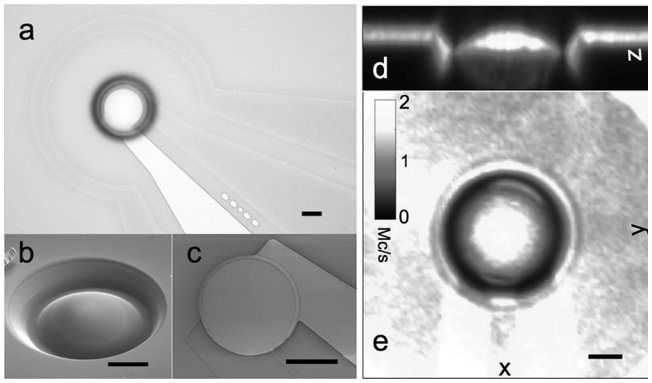

Figure 3: Micrographs and photoluminescence images of the finished device on an optical grade diamond substrate. (a) Device viewed from SIL side. (b) SEM of the milled solid immersion lens (radius of curvature 20 μm). (c) SEM of the transducer on the backside of the SIL. (d) and (e) show the photoluminescence image in a cross section view and a front view of the device (10 μm thick), collected using a home-built confocal microscope. The scale bars in all figures are 10 μm in length.

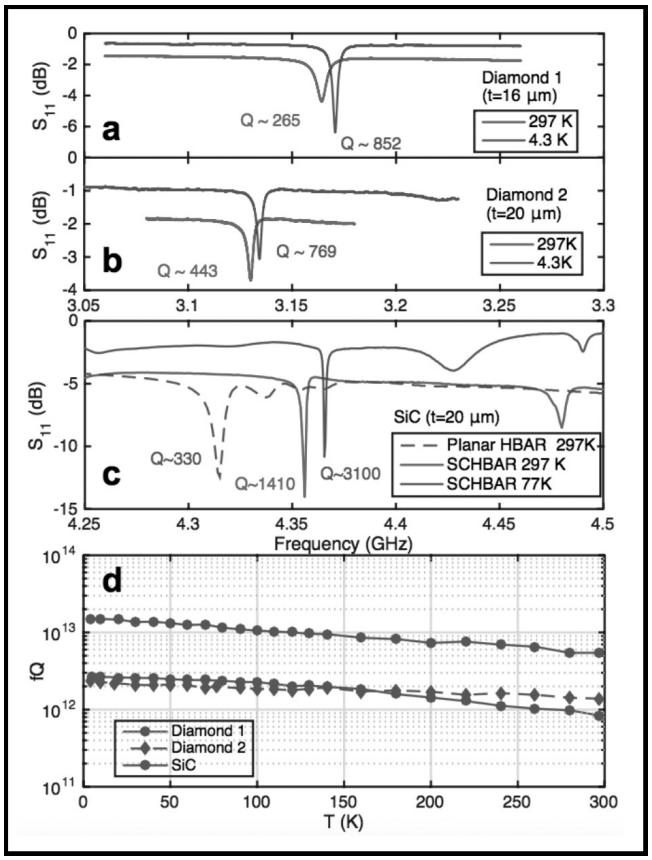

Figure 4: (a-c) S-parameters characterization of the device using a vector network analyzer. (d) Quality factors are extracted from the measured S-parameters as a function of temperature.

diamond for another 20- or 30-μm-deep etch on one side of the sample (etch rate 5 μm/hr). After lifting the quartz mask, we end up with a 10 μm or 20 μm diamond membrane suspended in a 40 μm frame. Atomic force microscopy (AFM) shows a surface roughness of < 0.3 nm.

A focused gallium ion beam (FIB, 30 kV, 20 nA) is used to mill the parabolic SIL structure on the diamond membrane. After FIB milling, the diamond surface is substantially graphitized and contains implanted gallium atoms (20 nm in depth). We then etch away the top 100 nm of damaged diamond using Ar/Cl_2 plasma, followed by a 120 nm O_2 plasma etch to oxygen terminate the diamond surface. A boiling tri-acid bath containing equal parts of sulfuric, nitric and perchloric acid is used to further clean off any residual contamination on the diamond. Optical profilometry and laser-scanning confocal microscopy have been used to confirm the profile accuracy of the SIL. The diamond membrane is then flipped with the planar side facing up. A piezoelectric zinc oxide (ZnO) transducer, consisting of bottom electrode (10 nm/90 nm Ti/Pt), 500 nm ZnO, top electrode (10 nm/180 nm Ti/Pt), and a microwave antenna are then lithographically defined and sputtered to finish the device fabrication.

We use a vector network analyzer (VNA) to characterize the scattering parameter (S-parameter) of the device. The mechanical quality factor of the device, Q, can be extracted from the VNA measurements. After mounting the devices in vacuum on a cold finger of a helium-flow cryostat, we perform electrical measurements as a function of temperature. The results are shown in Figure 4. The frequency and quality factor product is $f \cdot Q > 10^{12}$ for a 20-μm-thick diamond device at room temperature and $f \cdot Q > 10^{13}$ for a 20-μm-thick SiC device under cryogenic condition.

References:

[1] Chen, H; Opondo, N. F.; Jiang, B.; MacQuarrie, E. R.; Daveau R. S.; Bhave, S. A.; Fuchs G. D., arXiv: arXiv:1906.06309, 2019.

[2] Hadden, J.; Harrison, J.; Stanley-Clarke, A.; Marseglia, L.; Ho, Y.-L.; Patton, B.; O'Brien, J.; Rarity, J. Applied Physics Letters 2010, 97, 241901.

[3] Lee, C.; Gu, E.; Dawson, M.; Friel, I.; Scarsbrook, G. Diamond and Related Materials 2008, 17, 1292-1296.

[4] Friel, I.; Clewes, S.; Dhillon, H.; Perkins, N.; Twitchen, D.; Scarsbrook, G. Diamond and Related Materials 2009, 18, 808-815.

Coherent Spin-Magnon Coupling for Quantum-to-Quantum Transduction

CNF Project Number: 2126-12

Principal Investigator(s): Gregory D. Fuchs[1]

User(s): Hil Fung Harry Cheung[2]

Affiliation(s): 1. School of Applied and Engineering Physics, 2. Department of Physics; Cornell University

Primary Source(s) of Research Funding: Department of Energy (Grants No. DE-SC0019250)

Contact: gdf9@cornell.edu, hc663@cornell.edu

Website: http://fuchs.research.engineering.cornell.edu

Primary CNF Tools Used: GCA 5x stepper, AJA sputtering deposition system, P10 profilometer, Westbond 7400A ultrasonic wire bonder, Veeco Icon atomic force microscope, JEOL JBX-6300FS 100 kV electron-beam lithography system, PT770 etcher

Abstract:

Nitrogen-vacancy (NV) centers possess long spin coherence lifetimes and coherent optical transitions at low temperatures. The combination of long-lived ground state spins and a narrow optical transition is useful for quantum-to-quantum transduction between spins and photons and quantum entanglement between NV spins and photons have been demonstrated. Here, we are developing an interface between magnons and NV spins, which is a key link in a quantum network.

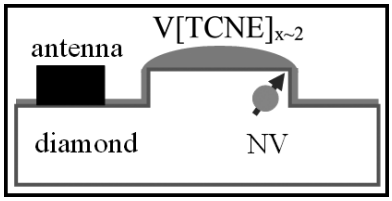

Figure 1: Schematic of coherent coupling between spins and magnons through an NV spin coupling to a magnon mode in V[TCNE]$_{x\sim2}$.

Summary of Research:

A key requirement in building a quantum network is the ability to transduce quantum information from one quantum system to another quantum system [1]. Diamond NV centers have long spin coherence time and a narrow linewidth optical transition, enabling both spin-photon entanglement [2,3] and spin-spin entanglement via photons [3]. NV centers are also suitable for quantum-to-quantum transduction between photons and magnons.

We are developing a platform that coherently couples microwave magnons to NV spins through magnetic dipole interaction. For this platform to perform quantum transduction, the magnons and spins decoherence rates need to be smaller than the coupling rate between magnons and spins. To enhance the coupling, the NV spin needs to be close (~ 30 nm) to the magnetic material (see Figure 1 for a schematic). To reduce magnon decoherence, we work with a low loss organic based magnetic material vanadium tetracyanoethylene (V[TCNE]$_{x\sim2}$) [4] in collaboration with Prof. Johnston-Halperin's group at Ohio State University (OSU).

Diamond polishing results in a highly strained surface, which increases near surface NV centers decoherence. This can be mitigated by etching away the first several microns of diamond using reactive ion etch (RIE) [5,6]. We compare the diamond surface before and after the stress relief etch using the PT770 etcher and observe a significant decrease in polishing streaks and surface roughness (Figure 2).

The spin-magnon coupling strength is maximized when the NV is aligned with the magnon mode. One approach to improve alignment is to etch the diamond with disks like structures and the grown magnetic material will be automatically aligned with the diamond structure. In order to optimize disks dimension and material growth condition, we fabricate SiO_2 arrays as test targets with diameters ranging from 200 nm to 8000 nm using electron beam lithography. The SiO_2 disks will also be used as shadow masks for diamond etching. Our collaborators at OSU have grown V[TCNE]$_{x\sim2}$ films on these disks showing nucleation free growth (Figure 3).

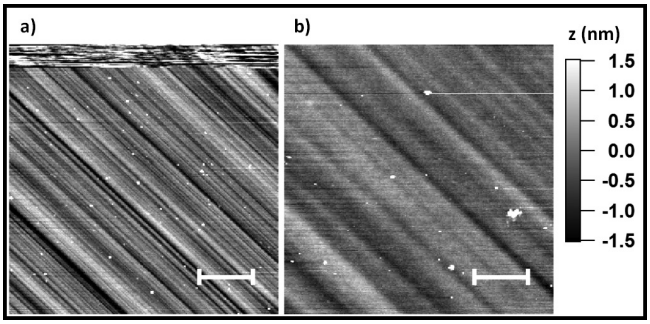

Figure 2: AFM image of the diamond before (a) and after (b) Ar/Cl_2 reactive ion etch. Scale bar is 1 μm.

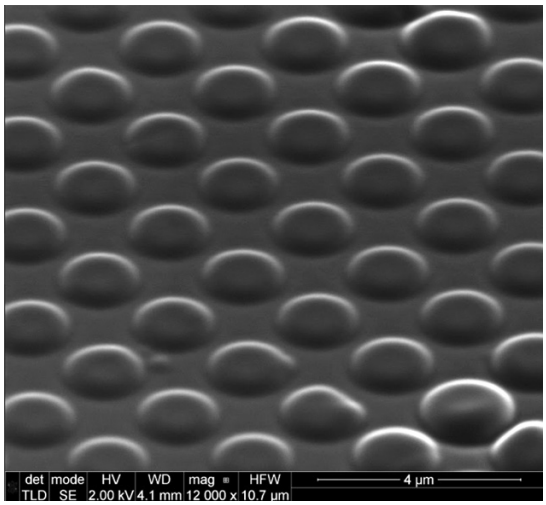

Figure 3: SEM of $V[TCNE]_{x\sim2}$ grown on 1 μm SiO_2 disks.

References:

[1] H. J. Kimble, "The quantum internet" Nature 453, 1023 (2008).

[2] E. Togan, et al. "Quantum entanglement between an optical photon and a solid-state spin qubit." Nature 466, 730 (2010).

[3] B. Hensen, et al. "Loophole-free Bell inequality violation using electron spins separated by 1.3 kilometres" Nature 526, 682 (2015).

[4] N. Zhu, et al. "Low loss spin wave resonances in organic-based ferrimagnet vanadium tetracyanoethylene thin films" Appl. Phys. Lett. 109, 082402 (2016).

[5] Y. Chu, et al. "Coherent optical transitions in implanted nitrogen vacancy centers" Nano Lett. 14, 982 (2014).

[6] S. Sangtawesin, et al. "Origins of diamond surface noise probed by correlating single spin measurements with surface spectroscopy" ArXiv: 1811.00144 (2018).

Optical Properties of Locally Strained WSe_2 Monolayers

CNF Project Number: 2126-12

Principal Investigator(s): Gregory D. Fuchs

User(s): Raphael Sura Daveau

Affiliation(s): Applied and Engineering Physics, Cornell University

Primary Source(s) of Research Funding: Air Force Office of Scientific Research

Contact: gdf9@cornell.edu, rsd228@cornell.edu

Website: http://fuchs.research.engineering.cornell.edu

Primary CNF Tools Used: JEOL 6300 electron-beam writer, GCA 5x stepper, Oxford 81 etcher

Abstract:

We investigate spectral properties of locally strained tungsten diselenide (WSe_2) monolayers. The local strain is created by layering the WSe_2 monolayer over a silicon dioxide (SiO_2) substrate pre-patterned with 150 nm-wide nanopillars. From spectral measurements, we show that strain shrinks the band gap resulting in local wells that concentrate carriers and redshifts the exciton recombination energy. Low temperature measurements show that the strain gradient is so far insufficient to create quantum confinement of carrier to generate single-photon emission.

Summary of Research:

Monolayer transition metal dichalcogenides (TMD) are direct bandgap semiconductors with a very strong light-matter interaction, large excitonic effects and possessing a new electronic degree of freedom, known as valley, that locks excitons to a given photon helicity [1]. Tungsten diselenide (WSe_2) is one such TMD, which has been shown to host quantum emitters [2]. Applications of quantum emitters inheriting valley properties are numerous, including dynamic generation of flying qubits with orthogonal polarization. While most reported emitters in WSe_2 monolayers are located at random, few reports show deterministic activation of quantum emitters via local strain by placing the WSe_2 monolayer over a patterned substrate [3]. The strain locally bends the band gap and creates quantum confinement of charge carriers, eventually leading to the emission of single photons upon recombination. Here, we report on the fabrication of nanopillar-patterned substrates, transfer and successful local straining of WSe_2 monolayers. We quantify the effect of strain on the band gap of WSe_2 at room temperature, while measurements at cryogenic temperatures remain elusive to resolve quantum emitters.

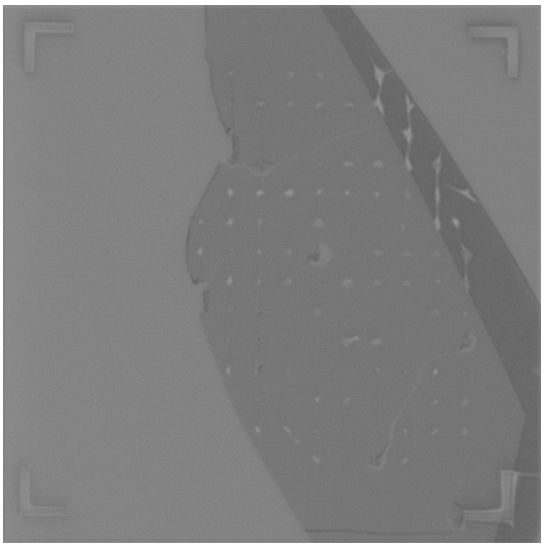

Figure 1: Optical microscopy image of a WSe_2 monolayer transferred over an array of nanopillars. Bright spots indicate tenting sites resulting in local strain in the WSe_2 monolayer.

The nanopillars are fabricated on a SiO_2 substrate via electron-beam lithography (JEOL 6300) using hydrogen silsesquioxane (HSQ) negative resist. The nanopillars are cylindrical with equal height and diameter of 150 nm. The spacing between pillars is 3 μm, which gives enough room for the WSe_2 monolayer to both conform to the pillars while layering on the substrate. To place an exfoliated WSe_2 monolayer deterministically over the fabricated nanopillars, we employ an all-dry transfer technique using polydimethylsiloxane (PDMS) stamps. Figure 1 shows an optical microscopy image of a mechanically exfoliated WSe_2 monolayer transferred on top of a nanopillar array. The tenting of the monolayer over the pillars is visible as bright spots due to increased contrast. Atomic force microscopy imaging confirms the conforming of the monolayer to the substrate and nanopillars.

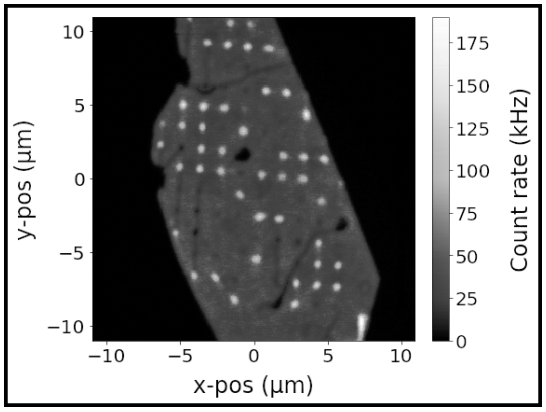

Figure 2: Room temperature photoluminescence scan of the WSe_2 monolayer displaying brighter spots at the nanopillar sites.

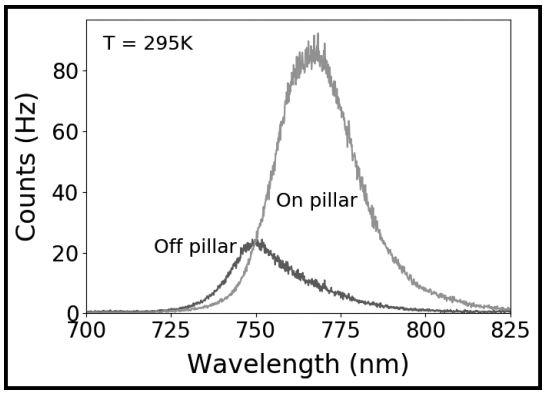

Figure 3: Spectrum of strained and unstrained WSe_2 monolayer. Besides brightness increase, a clear redshift of the emission at the pillar indicates strain that shrinks the band gap.

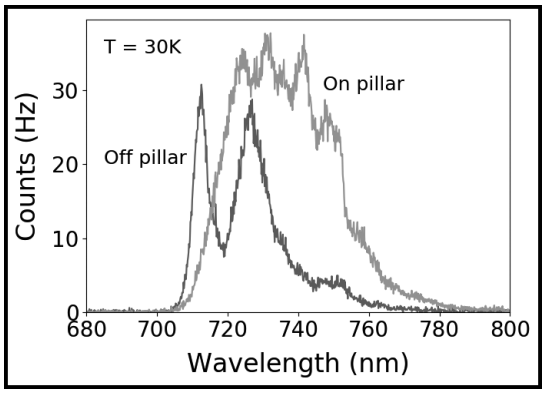

Figure 4: Spectrum of WSe_2 monolayer at T = 30 K. Besides the global redshift, no sharp features characteristic of quantum emitters are observed.

As-transferred WSe_2 monolayers necessitate no further treatment to be investigated optically. We perform spectral and micro-photoluminescence measurements in a confocal setup. Charge carriers are excited with a continuous wave laser at 532 nm with a power density of about 100 nW/µm^2. In the photoluminescence scan of Figure 2, we see a clear brightness increase at the pillar sites, indicating a larger carrier concentration. The strain shrinks the bandgap at the nanopillar sites, thus creating a local well where carriers get concentrated. This is consistent with the results of Figure 3, which shows a redshift of the exciton recombination energy by 35 meV (16 nm) at strained sites compared to unstrained WSe_2. For comparison, this is twice the value reported by Palacios-Berraquero, et al., in [3], which is promising for obtaining quantum emitters.

Quantum emitters in WSe_2 monolayers can only be resolved at cryogenic temperatures. We place the sample in a helium-flow cryostat and cool the sample to 30 K.

As shown in Figure 4, the emission of the unstrained WSe_2 is composed of the neutral exciton at 715 nm, negatively charged excitons at 735 nm and an additional peak at longer wavelengths originating from impurity-bound excitons [3]. At the pillar sites where the WSe_2 is strained, the spectrum is globally redshifted and is broadened towards longer wavelengths due to various local exciton traps naturally more populated at low temperatures. This data does not show correlation between strained sites and sharp emission lines characteristic of single quantum emitters. The temperature of the experiment is likely too high and resulting in a thermal depopulation of narrow exciton traps.

We conclude that the strain gradient created by the pillars is either too weak and/or too broad to confine a single exciton at 30 K but should be sufficient at temperatures below 10 K according to previous reports. Additionally, residual charging of the nanopillars from the electron beam during fabrication might quench the quantum emitters. Future generation of substrates will include electrical gating of the WSe_2 monolayer to control the charge environment of the emitters.

References:

[1] K. F. Mak and J. Shan, Nat. Photonics 10, 216 (2016).

[2] A. Srivastava, M. Sidler, A. V. Allain, D. S. Lembke, A. Kis and A. Imamo.lu, Nat. Nanotechnology 10, 1038 (2015).

[3] C. Palacios-Berraquero, D. M. Kara, A. R.-P. Montblanch, M. Barbone, P. Latawiec, D. Yoon, A. K. Ott, M. Loncar, A. C. Ferrari and M. Atature, Nat. Comm. 8, 15093 (2017).

Micrometer-Scale Graphene-Based Hall Sensors with Tunable Sensitivity

CNF Project Number: 2361-15

Principal Investigator(s): Katja C. Nowack

User(s): Brian T. Schaefer

Affiliation(s): Laboratory of Atomic and Solid-State Physics, Department of Physics; Cornell University

Primary Source(s) of Research Funding: Cornell Center for Materials Research with funding from the NSF MRSEC program (DMR-1719875), National Science Foundation Graduate Research Fellowship under Grant No. DGE-1650441

Contact: kcn34@cornell.edu, bts72@cornell.edu

Website: http://nowack.lassp.cornell.edu/

Primary CNF Tools Used: Veeco Icon AFM, Zeiss Supra SEM/Nabity, Trion etcher, 5x stepper, Oxford 81, Plasma-Therm VersaLine, odd-hour evaporator

Abstract:

We have fabricated high-quality graphene-based Hall sensors that can be tuned to maintain high magnetic field sensitivity at cryogenic temperatures, at room temperature, and in high background magnetic field. At best, we achieve a sensitivity of 80 nT $Hz^{-½}$, outperforming existing Hall sensor technologies. We will soon fabricate these devices into scanning probes to study magnetism and superconductivity via micrometer-scale magnetic imaging.

Summary of Research:

In a Hall-effect sensor, the deflection of current in a small magnetic field *B* produces a voltage response that is linear in *B* and large at low carrier density. The noise in the Hall voltage measurement ultimately determines the magnetic field sensitivity and is typically limited by instrumentation, Johnson, and low-frequency charge noise [1,2]. The requirements for large voltage response and low noise suggest a material with low carrier density and high mobility [1,3]. Whereas mobility decreases at low carrier density in most two-dimensional electron systems, in graphene the mobility is enhanced in the absence of long-range impurity scattering [4]. We exploit tuning the carrier density in graphene through electrostatic gating to maintain sensitivity in a wide range of temperature and magnetic field conditions.

To obtain the cleanest possible graphene devices (Figure 1), we adopt recently developed strategies to achieve record-low charge inhomogeneity in graphene: encapsulation in hexagonal boron nitride (hBN) gate dielectrics [5] and few-layer graphite (FLG) gate electrodes [6]. The low charged defect density in hBN and FLG [6] improve carrier mobility [5] and have the potential to reduce noise [7]. We use electron-beam lithography (Zeiss Supra, Nabity), plasma etching (Trion), and electron-beam evaporation to define the device shape and deposit metal (Cr/Au) contacts. The two-point resistance of the device increases sharply as we apply top gate voltage V_g to tune the carrier density through charge neutrality point (Figure 1b).

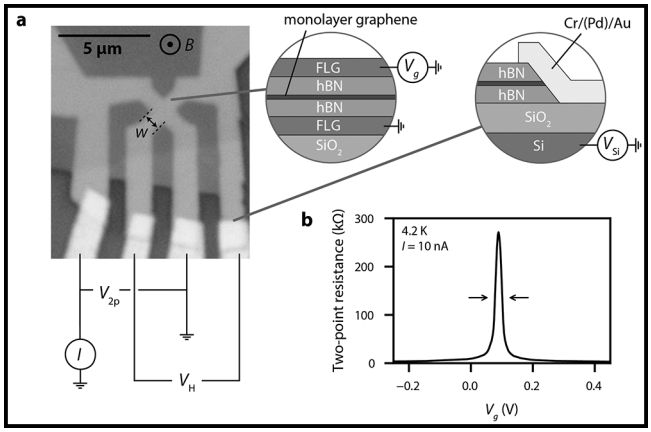

Figure 1: (a) Optical micrograph of a w = *1 µm Hall sensor. Upper inset: Layer structure consisting of graphene encapsulated with hexagonal boron nitride (hBN) and few-layer graphite (FLG). Lower inset: Edge contacts to part of the graphene extending outside of the FLG-gated region. (b) Top gate dependence of the two-point resistance* $R_{2p} = V_{2p}/I$.

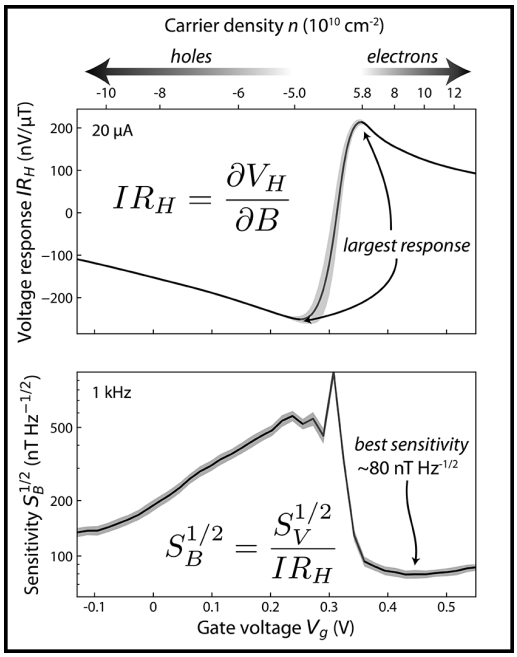

Figure 2: Gate voltage dependence of the Hall coefficient (top panel) and magnetic field sensitivity (bottom panel).

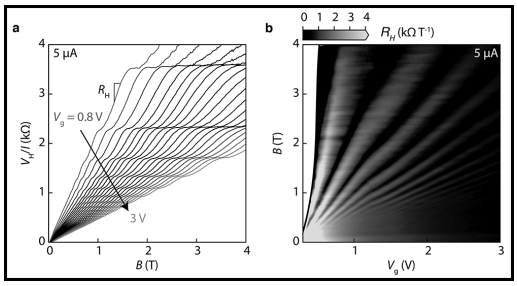

Figure 3: (a) Magnetic field dependence of the Hall resistance in the quantum Hall regime for a series of gate voltages. (b) Map of the Hall coefficient versus magnetic field and gate voltage.

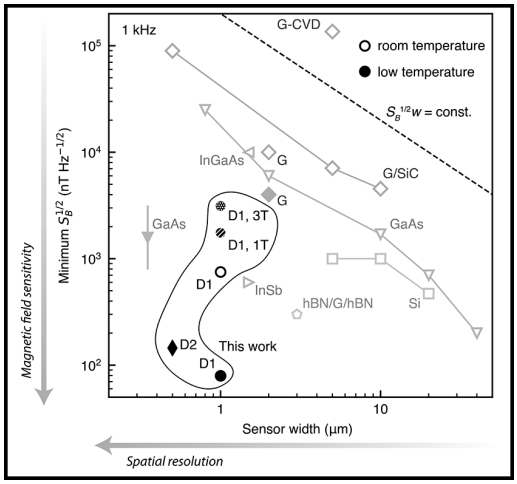

Figure 4: Magnetic field sensitivity $S_B^{1/2}$ at 1 kHz compared against the width w *of Hall sensors reported here and in the literature. Filled (open) markers correspond to liquid-helium (room) temperature. The outlined group of markers shows the best performance of our devices, and the other markers are estimates of the best performance of devices made from graphene and conventional semiconductor materials.*

To properly characterize the sensitivity of the devices to small changes in magnetic field [1,3], we apply a DC bias current and determine the Hall coefficient $R_H = I^{-1} [\partial V_H/\partial B]_{B=0}$ and Hall voltage noise spectral density $S_V^{1/2}$. The latter is dominated by flicker noise, which is pervasive in graphene-based microdevices [2] and decreases as $1/f^{1/2}$ with frequency f. The noise at 1 kHz is largest at low carrier density, at which charge fluctuations are poorly screened and the device resistance is large.

Dividing the Hall voltage noise by the Hall coefficient, we estimate the magnetic field sensitivity $S_B^{1/2} = S_V^{1/2}/IR_H$ (Figure 2, bottom panel). This quantity, when multiplied by the square root of the bandwidth of the measurement, represents the minimum detectable magnetic field. The best sensitivity — ~ 80 nT $Hz^{-1/2}$ — is found at an intermediate carrier density, indicating that the reduction in $S_V^{1/2}$ from tuning away from charge neutrality is more important than tuning to the largest R_H.

We also demonstrate for the first time that magnetic field response can be maintained in a large background magnetic field. While at low magnetic field, the Hall voltage grows linearly with magnetic field, above ~ 500 mT (at 5 μA bias) the Hall voltage begins to develop plateaus, indicating a transition into the quantum Hall regime (Figure 3a). At each (B, V_g), we calculate the effective Hall coefficient $R_H = I^{-1}(\partial V_H/\partial B)$ and plot as a map in Figure 3b, in which dark bands indicate suppressed Hall coefficient due to the plateaus. At a fixed magnetic field, tuning the gate voltage into one of the white bands enables the sensor to maintain sensitivity in high magnetic field.

Finally, in Figure 4 we compare the noise measurements for our devices at low temperature and room temperature against similar measurements on leading micrometer-scale Hall sensors reported in the literature. Our devices, which combine high magnetic field sensitivity with small sensor size, lie towards the lower left corner of the plot, outperforming all other reported materials. Our work establishes a new standard for fabricating Hall sensors to engineer superior device performance. We anticipate that scanning graphene-based magnetic field probes will enable the first high-resolution, high-sensitivity imaging of localized magnetic fields under high temperature and magnetic field conditions.

References:

[1] Dauber, J., et al. Ultra-sensitive Hall sensors based on graphene encapsulated in hexagonal boron nitride. Appl. Phys. Lett. 106, 193501 (2015).

[2] Balandin, A. A. Low-frequency 1/*f* noise in graphene devices. Nat. Nanotechnol. 8, 549-555 (2013).

[3] Hicks, C. W., Luan, L., Moler, K. A., Zeldov, E., and Shtrikman, H. Noise characteristics of 100 nm scale GaAs/$Al_xGa_{1-x}As$ scanning Hall probes. Appl. Phys. Lett. 90, 133512 (2007).

[4] Das Sarma, S., Adam, S., Hwang, E. H., and Rossi, E. Electronic transport in two-dimensional graphene. Rev. Mod. Phys. 83, 407-470 (2011).

[5] Wang, L., et al. One-dimensional electrical contact to a two-dimensional material. Science 342, 614-617 (2013).

[6] Zibrov, A. A., et al. Tunable interacting composite fermion phases in a half-filled bilayer-graphene Landau level. Nature 549, 360-364 (2017).

[7] Stolyarov, M. A., Liu, G., Rumyantsev, S. L., Shur, M., and Balandin, A. A. Suppression of 1/*f* noise in near-ballistic *h*-BN-graphene-*h*-BN heterostructure field-effect transistors. Appl. Phys. Lett. 107, 023106 (2015).

Gigahertz Surface Acoustic Waves on Periodically Patterned Layered Nanostructures

CNF Project Number: 2369-15

Principal Investigator(s): Brian C. Daly

User(s): Weili Cui

Affiliation(s): Physics Department, Astronomy Department; Vassar College, Poughkeepsie, NY

Primary Source(s) of Research Funding: National Science Foundation Award Division of Materials Research-1709521

Contact: brdaly@vassar.edu, weilicui@yahoo.com

Website: http://pages.vassar.edu/ultrafast/

Primary CNF Tools Used: E-beam lithography, CVD, thermal evaporation

Abstract:

We used the ultrafast pump-probe technique known as picosecond ultrasonics to generate and detect surface acoustic waves on nanoscale aluminum (Al) lines on silicon dioxide (SiO_2) on silicon (Si). In all cases we identified a Rayleigh-like surface acoustic wave with wavelength equal to the pitch of the lines and frequency in the range of 5-24 GHz. In some samples, we detected additional, higher frequency surface acoustic waves or independent modes of the Al lines with frequencies close to 50 GHz. Our new focus is on the effect of the probe beam polarization on which modes are detected.

Summary of Research:

In two recent papers, we have reported measurements of surface acoustic waves (SAWs) in periodically patterned nanostructures [1,2]. In these experiments we used an ultrafast optical pump-probe technique known as picosecond ultrasonics to generate and detect the SAWs. We then compared the experimental measurements to molecular dynamics simulations of the nanostructures in order to identify which modes we detected. In the second of these two papers, we measured samples that were fabricated at CNF and detected Rayleigh-like SAWs and Sezawa-like SAWs with wavelength equal to the pitch of Al lines that were etched on the sample. In some cases we also measured SAWs with wavelength equal to one-half or one-third of the pitch.

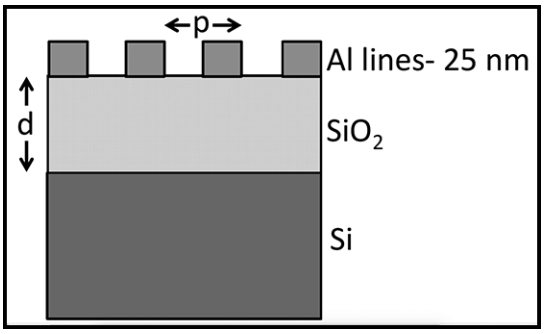

Figure 1: Schematic diagram of the samples. Film thickness d was either 60 nm or 112 nm as measured by picosecond ultrasonics. Al lines with pitch p varied from 1000 nm down to 140 nm. The duty cycle was close to 50% (+/- 10%) in all cases as measured by SEM imaging.

The ultrafast optical pump-probe experiment known as picosecond laser ultrasonics (PLU) has been described extensively in the literature [3]. We performed this experiment with a Ti:Sapphire oscillator operating at a 76 MHz repetition rate with pump wavelength of 800 nm and probe wavelengths of 800 nm or 400 nm. The 10 patterned samples that we studied are illustrated schematically in Figure 1. The samples were fabricated at the Cornell NanoScale Facility by the following process: thermal oxidation to produce the amorphous SiO_2 layer of thickness d = 60 or 112 nm, thermal evaporation of 25 nm of Al, and e-beam lithography and dry etching to create the nanometer scale Al pattern. The lines were etched perpendicular to the [110] direction in the Si substrate, they varied in pitch p ranging from 140 nm up to 1000 nm, and they were all etched near 50% (ranging from 40-60%) duty cycle. The patterned samples were placed into the optical setup, where pump and probe beams were both focused onto the same 20 μm diameter spot, so that anywhere from 20 to 140 periods of the pattern were strongly illuminated. The ultrafast pump pulses were absorbed by the Al lines, and the resulting rapid thermal expansion launched ultrasonic waves both

downward into the SiO_2 film and Si substrate, and laterally as SAWs in the direction perpendicular to the line pattern. The ultrasonic waves can be detected by the time delayed probe pulses due to transient changes in the reflectivity μR that they cause. The sources of these transient changes include the dependence of the optical constants of the Al on strain as well as the changes in reflectivity of the optical grating produced by the nanostructure as it responds to the acoustic oscillations. In this work, we focus on the signals caused by laterally propagating ultrasound and not the signals caused by acoustic waves traveling normal to the sample surface.

The conclusions about the types of surface acoustic waves we detected are described in Ref. 2. The next step in this project is to determine the impact of the polarization of the probe beam on the detection mechanism.

Figure 2 clearly demonstrates that for certain nanostructure periodicities, the polarization can dramatically effect which modes are detected. We are currently exploring this question computationally using a finite difference frequency domain (FDFD) calculation, and experimentally on a new set of samples to be fabricated at CNF this summer. We will pattern the Al lines on a sapphire substrate rather than a silicon substrate. The use of a transparent substrate will simplify the optical interaction of the probe beam with the sample and give us more insight into the mechanism behind the polarization effect.

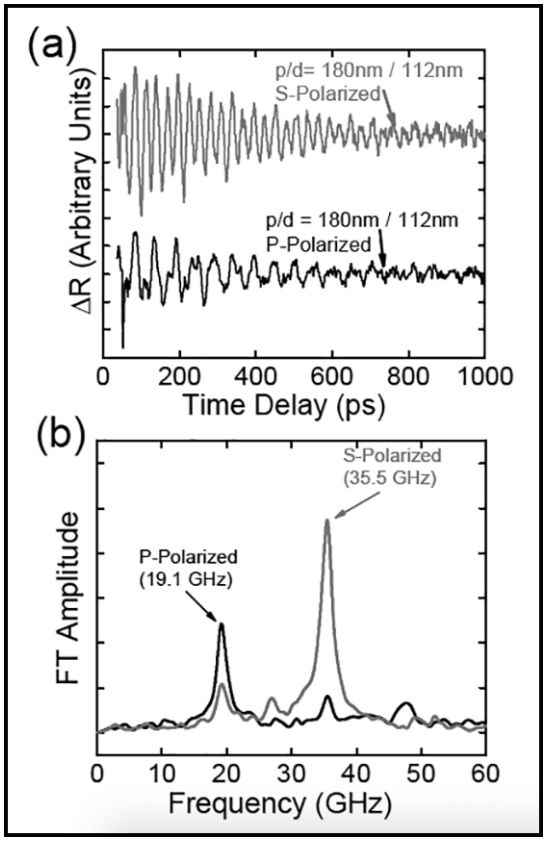

Figure 2: (a) μR for a sample with a pitch of 180 nm using 400 nm probe in the S-Polarized and P-polarized configurations. (b) Fourier transform amplitude of the signals in (a).

References:

[1] M.M. Bjornsson et al., J. Appl. Phys. 117, 095305 (2015).

[2] M. Colletta, et al., Ultrasonics 87, 126 (2018).

[3] C. Thomsen, H. T. Grahn, H. J. Maris, and J. Tauc, Phys. Rev. B 34, 4129 (1986).

Ultrafast Energy-Efficient Spin-Torque Magnetic Random Access Memories

CNF Project Number: 2444-16

Principal Investigator(s): Robert A. Buhrman

User(s): Lijun Zhu

Affiliation(s): School of Applied and Engineering Physics, Cornell University

Primary Source(s) of Research Funding: Office of Naval Research

Contact: rab8@cornell.edu, lz442@cornell.edu

Primary CNF Tools Used: ASML stepper, Veeco Icon, JEOL JBX-6300FS, ASML stepper, AJA sputtering

Abstract:

Spin-orbit torques [1-5] have been a hot topic in the research and technology communities due to their great promise for magnetic memories, oscillators and logic of post-Moore era. Here we demonstrate ultrafast energy-efficient magnetic random access memories (MRAMs) [6,7] fabricated at the Cornell NanoScale Science and Technology Facility.

Summary of Research:

We fabricated the spin-torque MRAM devices — schematically shown in Figure 1(a). The magnetic multilayer samples are patterned into three-terminal MRAM devices with a three-step procedure. First, we defined the spin Hall channel using DUV lithography (ASML stepper) and ion beam etching and measured the channel size to be 300 × 600 nm^2 by atomic force microscopy (Veeco Icon). We then defined the elliptical magnetic tunnel junction nanopillars with different aspect ratios and micron-size "via" pillars (as vertical connector between the bottom channel to top contact) onto the spin Hall channel with e-beam lithography (JEOL JBX-6300FS) and ion beam etching, and isolated the pillars with 80 nm thick SiO_2 deposited by an e-beam evaporator. Finally, contacts of Ti 5/Pt 50 were deposited on the top of the magnetic tunnel junction pillars and "via" pillars for electrical measurements by combining the DUV lithography (ASML stepper), AJA sputtering, and liftoff processes.

Figure 1(b) shows the characteristic switching behavior of the MRAMs as the write current in the spin Hall channel is ramped quasi-statically. The MTJs show abrupt switching at write currents of 20 μA. Since thermal fluctuations assist the reversal of a nanoscale MTJ device during slow current ramps, we carried out ramp rate measurements and determined that the zero-temperature switching current is 70 μA, The critical switching density in the Pt spin Hall channel is therefore $j_{C0} \approx 3.6 \times 10^7$ A/cm^2. Both the total critical switching and the low switching current density are the lowest yet reported for any spin-torque MRAMs. We also measured the fast switching behaviors of our spin-torque MRAMs and find deterministic switching even at 200 ps, which is also the fastest switching yet known.

References:

[1] L. Zhu, D.C. Ralph, R.A. Buhrman, Phys. Rev. Lett. 122, 077201 (2019).

[2] L. Zhu, K Sobotkiewich, X. Ma, X. Li, D.C. Ralph, R.A. Buhrman, Adv. Funct. Mater. 29, 1805822 (2019).

[3] L. Zhu, D.C. Ralph, R.A. Buhrman, Phys. Rev. B 99, 180404 (R) (2019).

[4] L.J. Zhu, D.C. Ralph, R.A. Buhrman, Phys. Rev. B 98, 134406 (2018).

[5] L. Zhu, D.C. Ralph, R.A. Buhrman, Phys. Rev. Appl. 10, 031001 (2018).

[6] L. Zhu, L. Zhu, S. Shi, M. Sui, D. C. Ralph, R. A. Buhrman, Phys. Rev. Appl. 11, 061004 (2019).

[7] L. Zhu, L. Zhu, S. Shi, D. C. Ralph, R. A. Buhrman, Energy-efficient Ultrafast SOT-MRAMs based on low-resistivity spin Hall metals $Au_{0.25}Pt_{0.75}$, in preparation.

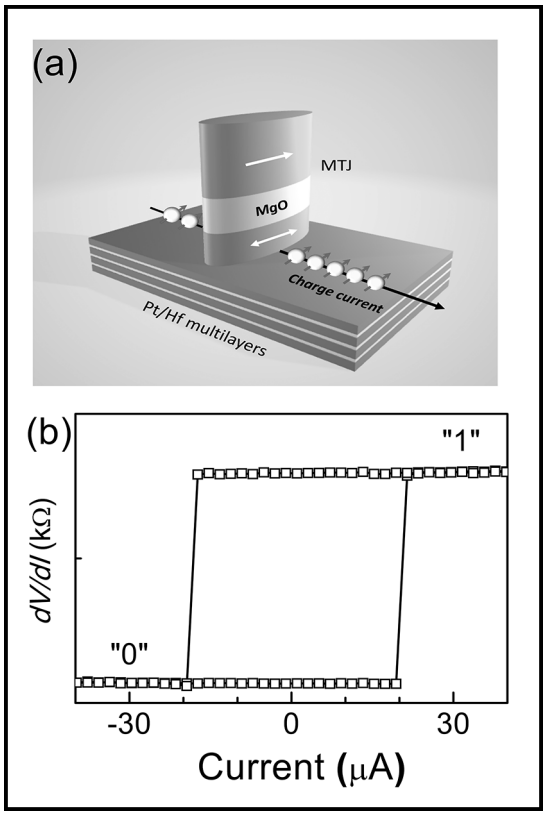

Figure 1: (a) Schematic of a spin-torque MRAM device; (b) Current-induced switching of the MRAMs.

Low Loss Photonic Packaging Using Fusion Splicing

CNF Project Number: 2524-17

Principal Investigator(s): Jaime Cardenas

User(s): Juniyali Nauriyal, Meiting Song

Affiliation(s): Department of Electrical and Computer Engineering, University of Rochester; The Institute of Optics, University of Rochester

Primary Source(s) of Research Funding: The Hajim School of Engineering and Applied Sciences, University of Rochester

Contract: jaime.cardenas@rochester.edu, j.nauriyal@rochester.edu

Primary CNF Tools Used: ASML stepper, Oxford 100, Oxford 82, Gamma, GSI, Furnace, Unaxis, Xetch, dicing saw

Abstract:

We present a novel photonic packaging method for permanent optical edge coupling between a fiber and chip using fusion splicing. We demonstrate minimum loss of 1.0 dB per-facet with 0.6 dB penalty over 160 nm bandwidth from 1480-1640 nm.

Summary of Research:

One of the biggest challenges in the silicon photonics industry is to permanently attach an optical fiber to a photonic chip, with high optical coupling efficiency. Multiple packaging methods have been demonstrated to increase the coupling efficiency between an optical fiber and a chip while increasing throughput for high volume manufacturing. Some of these methods use grating couplers to couple light from the top of the chip, but grating couplers are fundamentally bandwidth-limited while edge couplers use a form of waveguide taper and/or lensed fiber and are inherently broadband but require access to the sides of a chip and have tight misalignment tolerances [1]. When used in packaging applications, individual fibers and fiber arrays are permanently placed over grating couplers using optical adhesive and fixtures or ferrules. Optical adhesives shrink during curing and alignment tolerances are tight, it becomes challenging to achieve lower losses with high scalability.

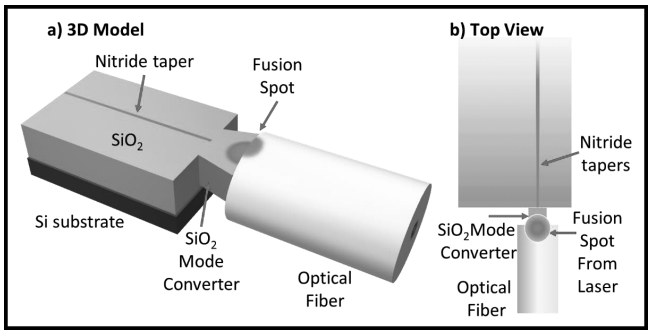

Figure 1: a) 3D model of a packaged device using silicon dioxide mode converter fused to SMF-28 fiber. It shows undercut silicon substrate which isolates the oxide mode converter from the chip, b) schematic representation of the top view of the method shows the fusion splicing spot from the CO_2 laser which improves the coupling efficiency.

We present a novel photonic packaging method for permanent optical edge coupling between a fiber and a photonic chip using fusion splicing which is low-cost, low-loss and scalable to high volume manufacturing [2]. We introduce a cantilever-type silicon dioxide mode converter which is mode matched to a single mode fiber at the input facet and a silicon nitride waveguide at the output facet [3-5]. The silicon dioxide mode converter is permanently fused to the optical fiber using a CO_2 laser (Figure 1) [5]. As the main components of an optical fiber are silicon dioxide same as the silicon dioxide cladding on the photonic chip, it readily absorbs 10.6 μm of radiative power from the laser and forms a permanent bond between the two interfaces. This packaging method is compatible with any photonic device with a cladding of silicon dioxide with different types of inverse nanotapers. The geometry of the oxide mode converter can be engineered to match the mode profile of the waveguide nanotaper. The proposed method is compatible with standard foundry processes and does not require any deviations from the standard fabrication process. The oxide mode converter uses two-stage mode conversion: first mode conversion from the waveguide (mode size < 1 μm) into the oxide mode converter and second, from the oxide mode converter to the optical fiber (mode size of 10.4 μm). The two sides of the oxide mode converter are engineered to maximize the coupling from the waveguide nanotaper to the cleaved optical fiber.

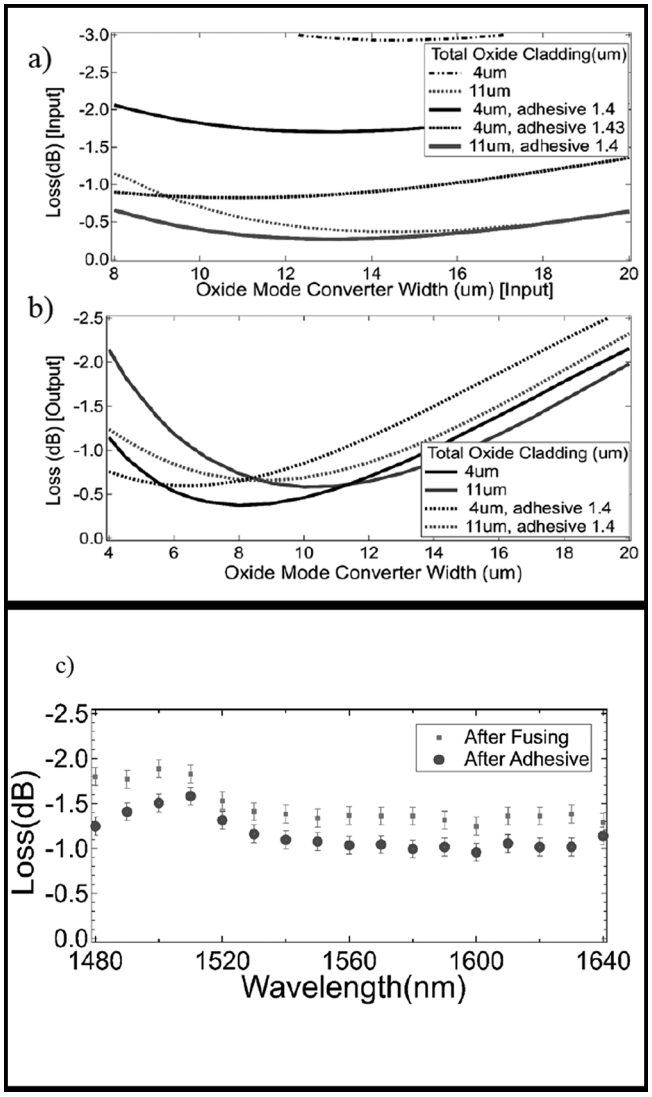

Figure 2: Coupling loss between the fiber and the mode converter as a function of oxide mode converter input width, a) at the input interface from the fiber to the mode converter, and b) from the mode converter into the waveguide. c) The coupling loss per-facet after fusing and after applying adhesive as a function of wavelength, a minimum loss of 1.0 dB is measured.

The width of the oxide mode converter is calculated with different total oxide cladding thickness (μm) (Figure 2a and b) with a fixed nitride waveguide taper width. Our simulations also show that a minimum coupling loss of 0.3 dB can be achieved with 14 μm oxide mode converter width and 11 μm total (top plus bottom) oxide cladding thickness with an adhesive of refractive index 1.4. The waveguide nanotaper is made of silicon nitride and is 0.18 μm wide at the tip and 100 μm long with a linear profile. We also calculated the 1 dB penalty in misalignment tolerance between the fiber and the oxide mode converter, which is +/- 2.5 μm and +/- 2.4 μm in horizontal and vertical directions respectively.

The devices were fabricated using standard CMOS compatible, microfabrication techniques. The waveguides were patterned using standard DUV optical lithography at 248 nm, the devices were etched using inductively coupled plasma reactive ion etcher and cladded oxide using plasma enhanced chemical vapor deposition. After dicing, we remove the silicon substrate underneath the oxide mode converter to optically isolate it. We fuse the SMF-28 cleaved fiber to the oxide mode converter using a CO_2 laser and reinforce the splice by adding an optical adhesive of suitable refractive index. Fusing the fiber and the chip together using radiative heating leaves no residue behind and forms a permanent bond.

We demonstrate a minimum loss of 1.0 dB per facet with a 0.6 dB penalty over 160 nm bandwidth near the C-band on a standard, cleaved SMF-28 fiber fused to the silicon nitride photonic chip (Figure 2c) [2]. We measure coupling loss after fusing and after the addition of optical adhesive of refractive index 1.3825.

We measure a -30.1 dB of optical return loss using a circulator for 1550 nm after fusing the optical fiber to the chip. The coupling loss before fusing was 2.1 dB with 0.4 dB of waveguide propagation loss. After fusing the fiber to the chip, the loss decreased to 1.3 dB on the fused facet and further decreases to 1.0 dB after the application of optical adhesive.

References:

[1] T. Barwicz, et al., A Novel Approach to Photonic Packaging Leveraging Existing High-throughput Microelectronic Facilities, IEEE J. Sel. Top. Quantum Electron. 22 1-12. doi:10.1109/JSTQE.2016.2593637 (2016).

[2] J. Nauriyal, M. Song, R. Yu, and J. Cardenas, "Fiber-to-chip fusion splicing for low-loss photonic packaging," Optica, OPTICA 6, 549-552 (2019).

[3] L. Chen, et al., Low-Loss and Broadband Cantilever Couplers Between Standard Cleaved Fibers and High-Index-Contrast SiN or Si Waveguides, IEEE Photonics Technol. Lett. 22, 1744-1746. doi:10.1109/LPT.2010.2085040 (2010).

[4] N. Shimizu, Fusion splicing between deposited silica waveguides and optical fibers, Electron. Commun. Jpn. Part Commun. 67, 115-122. doi:10.1002/ecja.4400670914 (n.d.).

[5] P. Pal, W.H. Knox, Low loss fusion splicing of micron scale silica fibers, Opt. Express. 16, 11568-11573. doi:10.1364/OE.16.011568 (2008).

Spin Tunnel Field-Effect Transistors Based on Two-Dimensional van der Waals Heterostructures

CNF Project Number: 2633-18

Principal Investigator(s): Jie Shan, Kin Fai Mak

User(s): Lizhong Li, Shengwei Jiang

Affiliation(s): Laboratory of Atomic and Solid State Physics, Applied and Engineering Physics; Cornell University

Primary Source(s) of Research Funding: National Science Foundation under award DMR-1807810 for the sample and device fabrication, the Office of Naval Research under award N00014-18-1-2368 for the device characterization, and the Air Force Office of Scientific Research Hybrid Materials MURI under award FA9550-18-1-0480 for optical measurements

Contact: jie.shan@cornell.edu, kinfai.mak@cornell.edu, sj538@cornell.edu, ll646@cornell.edu

Primary CNF Tools Used: Autostep i-line stepper, Hamatech wafer processor develop, Heidelberg mask writer DWL2000, photolithography spinners, SC4500 odd/even-hour evaporator, DISCO dicing saw

Abstract:

Transistors based on control of spin orientations, if realized, can revolutionize modern electronics through the implementation of faster and more energy efficient performance and non-volatile data storage. Recent development in magnetic switching by a gate voltage and magnetic reading by the spin filtering effect in two-dimensional magnets has inspired a new operational principle for spin transistors. In this project, we demonstrate a spin tunnel field-effect transistor based on dual-gated graphene/CrI_3 tunnel junctions.

Summary of Research:

Spin field-effect transistors (FETs) were first proposed by Datta and Das in 1990 [1]. These spin-based devices promise non-volatile data storage and faster and more energy-efficient performance than the current transistors. The original proposal that relies on electric-field-controlled spin precession in a semiconductor channel, faces significant challenges including inefficient spin injection, spin relaxation and spread of the spin precession angle. The recently discovered two-dimensional magnetic insulators [2,3] provide a unique platform to explore new spintronic device concepts. In this project, we develop a tunnel field-effect transistor (TFET) based on few-layer CrI_3 as a magnetic tunnel barrier to achieve spin-dependent outputs that are voltage controllable and reversible.

Figure 1 shows the device structure. It consists of a van der Waals heterostructure of bilayer graphene/bilayer CrI_3/bilayer graphene with top and bottom gates. The vertical tunnel junction utilizes bilayer graphene as the source and drain contacts and bilayer CrI_3 as the magnetic tunnel barrier. The two nearly symmetric gates are made of few-layer graphene gate electrodes and hexagonal boron nitride (hBN) gate dielectrics. The gates tune the Fermi level of the nearest bilayer graphene contact effectively, which modulates the conductance of the junction through resonant tunneling.

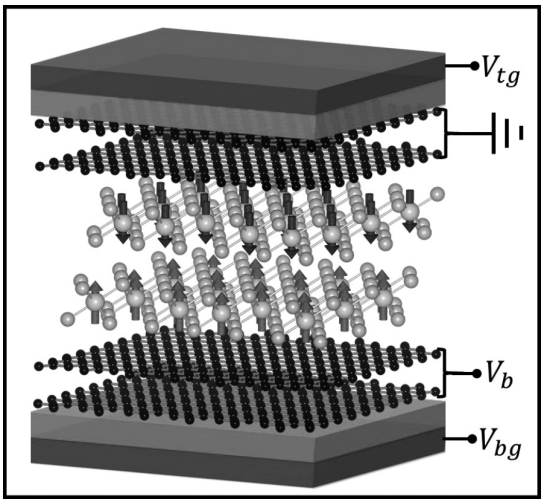

Figure 1: Operational principle of a spin TFET based on gate-controlled spin-flip transition in bilayer CrI_3 and spin filtering in the tunnel junction. Arrows indicate the spin orientation in CrI_3 layers.

The gates can also cause a significant modulation in the tunnel conductance by inducing a spin-flip transition in bilayer CrI_3 by an electric field or through electrostatic gating [4-6]. The conductance is high (low) when the spins in the two layers are aligned (misaligned) due to the spin-filtering effect [7,8]. A spin-TFET action is realized

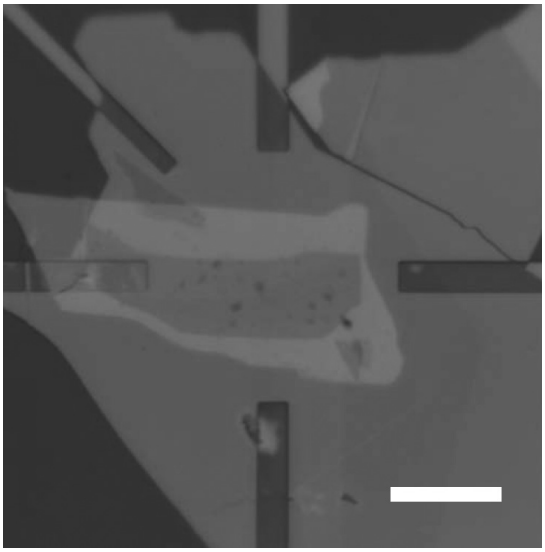

Figure 2: Optical images of a van der Waals heterostructure device deposited on pre-patterned electrodes.

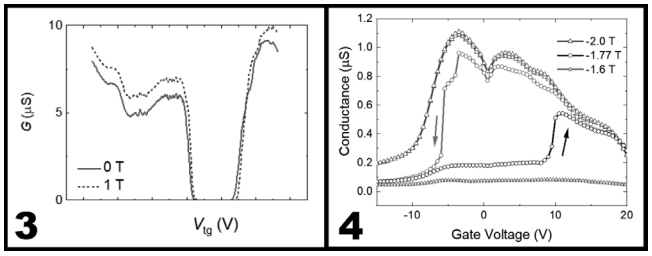

Figure 3, left: Gate dependence of the tunnel conductance in a bilayer CrI_3 device under an out-of-plane magnetic field of 0 T and 1 T [6].
Figure 4, right: Tunnel conductance of a TFET with a four-layer CrI_3 tunnel barrier is repeatedly switched by gating under a constant magnetic bias of -1.77 T. The top and bottom gate voltages are identical, and their sum is shown in the horizontal axis [6]. Results under -2.0 T and -1.6 T (corresponding to the barrier in the ferromagnetic and antiferromagnetic state, respectively) are included for comparison.

through electrical switching of spins in the magnetic tunnel barrier.

Figure 2 is an optical image of a typical device. The Ti/Au electrodes were first patterned on Si/SiO_2 substrates by photolithography and metal evaporation. Atomically thin samples of CrI_3, hBN, and graphene were first exfoliated from their bulk crystals onto silicon substrates covered with a 300 nm thermal oxide layer. The selected thin flakes of appropriate thickness and geometry were then picked up one-by-one by a stamp consisting of a thin layer of polycarbonate on polydimethylsiloxane. The complete stack was then deposited onto the substrates with pre-patterned Au electrodes.

An ambipolar transistor behavior with a zero conductance (i.e. off) state is observed for graphene tunnel junctions (solid line, Figure 3). This is a consequence of a sizable band gap opened in both bilayer graphene contacts by a built-in interfacial electric field from the asymmetric hBN/bilayer graphene/bilayer CrI_3 structure.

The TFET output is dependent on the magnetic state of the tunnel barrier. Under a vertical magnetic field of 1 T (dashed line, Figure 3), bilayer CrI_3 switches from an interlayer antiferromagnet to a ferromagnet. The gate dependence of the conductance shifts towards a slightly larger gate voltage, corresponding to a shift in the energy level alignment in the tunnel junction. The tunneling conductance increases over a large doping range.

We demonstrate the spin TFET action, i.e. control of the tunnel conductance by electrically switching the magnetic state of CrI_3. To minimize the trivial conductance, change due to electrostatic doping, we choose a range of gate voltage, where the conductance is weakly gate dependent.

Figure 4 shows the result for a 4-layer CrI_3 device under a constant magnetic bias (-1.77 T), which is slightly above the spin-flip transition [9]. The gate voltage can repeatedly alter the TFET between a high and a low conductance state. As a reference, we also include the conductance under a bias magnetic field much above or below the spin-flip transition.

A relative change of ~ 400% in the tunnel conductance with a large hysteresis has been achieved through gating. The switching is originated from a gate-dependent spin-flip transition field.

In conclusion, a new type of spin transistors is achieved, which relies on the spin filtering effect to inject and detect spin, and electrical switching of the magnetization configurations in the tunnel barrier.

References:

[1] Datta, S., and Das, B. Applied Physics Letters 56, 665 (1990).

[2] Huang, B., et al. Nature 546, 270 (2017).

[3] Gong, C., et al. Nature 546, 265-269 (2017).

[4] Jiang, S., Shan, J., and Mak, K. F. Nature Materials 17, 406 (2018).

[5] Jiang, S., Li, L., Wang, Z., Mak, K. F., and Shan, J. Nature Nanotechnology 13, 549 (2018).

[6] Huang, B., et al. Nature Nanotechnology 13, 544 (2018).

[7] Song, T., et al. Science 360, 1214-1218 (2018).

[8] Klein, D. R., et al. Science 360, 1218-1222 (2018).

[9] Jiang, S., Li, L., Wang, Z., Shan, J., and Mak, K. F. Nature Electronics 2, 159 (2019).

Non-Linear Anomalous Hall Effect in Few-Layer WTe_2

CNF Project Number: 2633-18

Principal Investigator(s): Jie Shan, Kin Fai Mak

User(s): Kaifei Kang, Egon Sohn, Tingxin Li

Affiliation(s): Department of Applied and Engineering Physics, Cornell University

Primary Source(s) of Research Funding: Army Research Office, US Department of Energy (Office of Basic Energy Sciences), National Science Foundation

Contact: kinfai.mak@cornell.edu, kk726@cornell.edu, es799@cornell.edu, tl684@cornell.edu

Primary CNF Tools Used: Zeiss Supra SEM, Pt 720-740 reactive ion etcher, Autostep i-line stepper, SC4500 odd/even-hour evaporator

Abstract:

The Hall effect occurs only in systems with broken time-reversal symmetry, such as materials under an external magnetic field in the ordinary Hall effect and magnetic materials in the anomalous Hall effect (AHE). Here we demonstrate a new Hall effect in a non-magnetic material, few-layer T_d-WTe_2 under zero magnetic field. In this effect, the Hall voltage depends quadratically on the longitudinal current. Our results open the possibility of exploring topological effects in solids by nonlinear electrical transport and applications of the phenomenon in spin-orbit torque devices.

Summary of Research:

The linear Hall effect is odd under time-reversal operation, it occurs only in systems with broken time-reversal symmetry (TRS). The second-order nonlinear effect, in which the Hall voltage depends on drive current quadratically, however, is even under time-reversal operation. It therefore does not require the application of an external magnetic field or the presence of magnetic order in the material. Furthermore, the effect is odd under space-inversion operation and is thus limited to systems with broken inversion symmetry. More specifically, the nonlinear anomalous Hall effect (AHE) has been predicted to exist in crystals with a polar axis and can be used to probe the topological properties of the solids such as the Berry curvature dipole [1]. The experimental studies of the nonlinear AHE remain elusive.

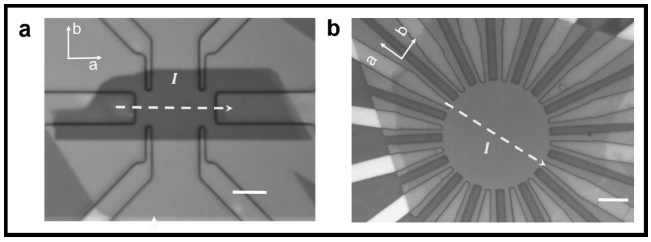

Figure 1: Optical image of a typical Hall bar (top) and circular disk (bottom) device used in this study. The scale bars are 5 m. WTe2 samples are in grey, Pt electrodes in orange, and the Si substrate in dark red-orange for the disk device, respectively. Dashed yellow lines indicate the current (I) direction. a and b are the crystal axes.

Here we investigate the nonlinear electrical properties of metallic few-layer T_d-WTe_2. Atomically thin T_d-WTe_2 has one polar axis along the crystal b axis, and thus allows the nonlinear AHE. Figure 1 shows the images of samples employed in the experiment. Figure 1a is a sample in the Hall bar geometry and the Figure 1b shows a sample in the circular disk shape. To fabricate these devices, few-layer WTe_2 and hexagonal boron nitride (hBN) were mechanically exfoliated from bulk crystals (HQ Graphene) onto silicon substrates. The hBN and WTe_2 flakes were picked up by a stamp consisting of a thin film of polycarbonate (PC) on polydimethylsiloxane (PDMS). The stack was then released onto a Si substrate with pre-patterned Pt electrodes. For disk devices, the completed stack was further patterned into a circular shape. To this end, a poly(methyl methacrylate (PMMA) mask with desired shape was first defined by standard e-beam lithography on top of the completed stack, it was then etched by reactive ion etching with SF_6 gas. Finally the residual PMMA was removed in an acetone bath.

To measure the nonlinear anomalous Hall effect in few-layer WTe_2 in the Hall bar devices, we apply an AC current along the crystal a-axis at a fixed frequency (137 Hz) and measure the longitudinal and transverse voltage drops at both the first and second-harmonic frequencies. The circular disk devices were measured in the same fashion. Current was injected from one of the 16 electrodes,

voltages parallel and perpendicular to the current injection were recorded. The angular dependence of the nonlinear anomalous Hall effect was carried out by rotating both current injection and voltage measurement simultaneously.

A second-harmonic transverse $V_{\perp}^{2\omega}$ voltage was observed in both the Hall bar and circular disk devices. Its magnitude scales quadratically with the current. In the disk devices, the normalized nonlinear hall response $V_{\perp}^{2\omega}/(V_{||})^2$ (where $V_{||}$ is the linear longitudinal voltage) shows a one-fold angular dependence (Figure 2). It maximizes when the current is perpendicular to the mirror line (i.e. along the a-axis), and minimizes when the current is parallel to the mirror line (i.e. along the b-axis). The observed effect is fully consistent with the crystal symmetry of few-layer T_d-WTe_2.

The microscopic mechanism of the observed effect was further examined by studying its scaling against scattering (conductivity σ).

The normalized nonlinear Hall response

$$\frac{E_{\perp}^{2\omega}}{(E_{\parallel})^2}$$

(where $E_{\perp}^{2\omega}$ and $E_{||}$ are the fields calculated from the corresponding voltages and the device dimensions) was observed to scale linearly with σ^2 for a large range of temperature (Figure 3). Such a scaling law suggests that the observed nonlinear Hall effect can be understood as an anomalous Hall effect with electrically generated magnetization. Our result also indicates that both intrinsic Berry curvature dipole and extrinsic spin-dependent scatterings contribute to the observed nonlinear AHE.

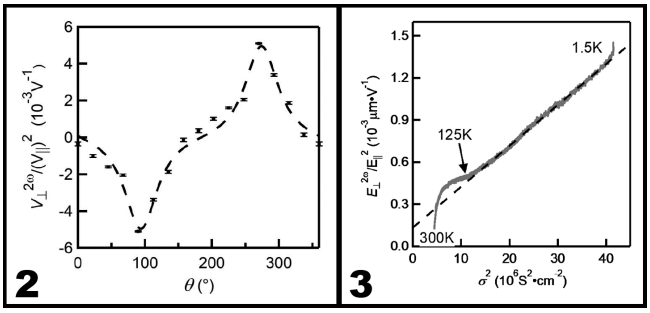

Figure 2, left: The nonlinear Hall effect as a function of current angle. Symbols are experimental data and the dashed line is a fit to the nonlinear response model including all second-order nonlinear susceptibilities allowed by the crystal symmetry. Figure 3, right: The normalized nonlinear Hall effect as a function of square of the longitudinal conductivity. The dashed line is a linear fit.

References:

[1] Sodemann, I., and Fu, L. Quantum Nonlinear Hall Effect Induced by Berry Curvature Dipole in Time-Reversal Invariant Materials. Physical Review Letters 115, 216806 (2015).

Mass Transport on Graphene

CNF Project Number: 2767-19
Principal Investigator(s): Scott Schiffres
User(s): Yingchun Jiang

Affiliation(s): Mechanical Engineering, Binghamton University
Primary Source(s) of Research Funding: Startup funding
Contact: sschiffr@binghamton.edu, yjiang89@binghamton.edu
Primary CNF Tools Used: Photolithography tools, ABM contact aligner, Zeiss Ultra SEM

Summary of Research:

The development of nanotechnology requires versatile manipulation tools for atomic scale assembly and controlled material delivery. Scanning tunneling microscope (STM), atomic force microscope (AFM) have been demonstrated as powerful tools for manipulation atoms and molecules on clean surfaces. However, these tools suffer from low delivery efficiency: they are not capable to deliver nanometer scale features containing large amounts of atoms, and they cannot deliver atom efficiently to desired work area (sticky).

Carbon nanotubes and graphene have been suggested as possible nanoscale mass conveyors with electric field as source of applied force. Controllable and reversible atomic metal transportation along carbon nanotubes (CNTs) and transport of more than 10^7 atoms have been demonstrated [1-3]. Graphene is mechanically robust and chemically inert; it can sustain large current density similar to CNTs. It has advantage over CNTs that more complicated mass transport circuits can be designed with lithography techniques[4-7].

Despite experiments that show the Al plate transport along graphene in crossroad configuration, the more complicated transport circuit and the other type of transport species, and atomic scale transport are needed to be tested. Theoretical model on the nature of the driving mechanism will also be developed.

References:

[1] B.C. Regan, S. Aloni, R.O. Ritchie, U. Dahmen, A. Zetti, Carbon nanotubes as nanoscale mass conveyors, Nature. 428 924-927. doi:10.1038/nature02496 (2004).

[2] Z. Ren, Y. Lan, Y. Wang, Subnanometer motion of cargoes driven by thermal gradients along carbon nanotubes, Science (80-.). 7-43. doi:10.1007/978-3-642-30490-3_2 (2012).

[3] N. Mingo, L. Yang, J. Han, Current-induced forces upon atoms adsorbed on conducting carbon nanotubes, J. Phys. Chem. B. 105 11142-11147. doi:10.1021/jp011491s (2001).

[4] S. Hertel, F. Kisslinger, J. Jobst, D. Waldmann, M. Krieger, H.B. Weber, Current annealing and electrical breakdown of epitaxial graphene, Appl. Phys. Lett. 98 2009-2012. doi:10.1063/1.3592841 (2011).

[5] A. Barreiro, R. Rurali, E.R. Hernández, A. Bachtold, Structured graphene devices for mass transport, Small. 7 775-780. doi:10.1002/smll.201001916 (2011).

[6] J. Moser, A. Barreiro, A. Bachtold, Current-induced cleaning of graphene, Appl. Phys. Lett. 91 1-4. doi:10.1063/1.2789673 (2007).

[7] D. Solenov, K.A. Velizhanin, Adsorbate transport on graphene by electromigration, Phys. Rev. Lett. 109 1-5. doi:10.1103/PhysRevLett.109.095504 (2012).

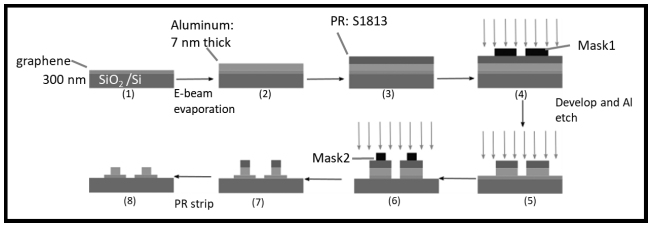

Figure 1: Process flow for making Al pads on graphene by Al etching.

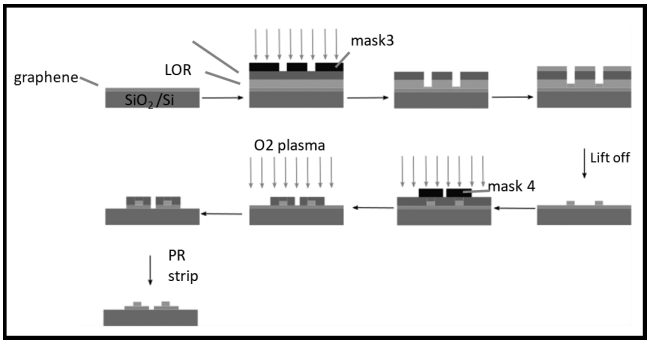

Figure 2: Process flow for making Al pads on graphene ribbon by lift off.

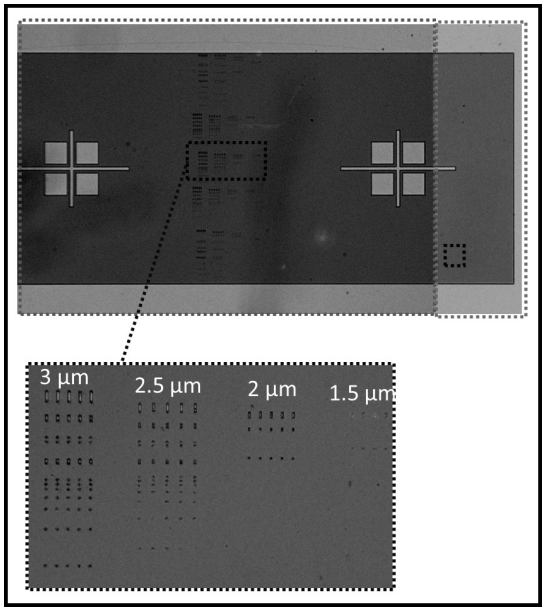

Figure 3: Al pads on graphene before stripping photoresist.

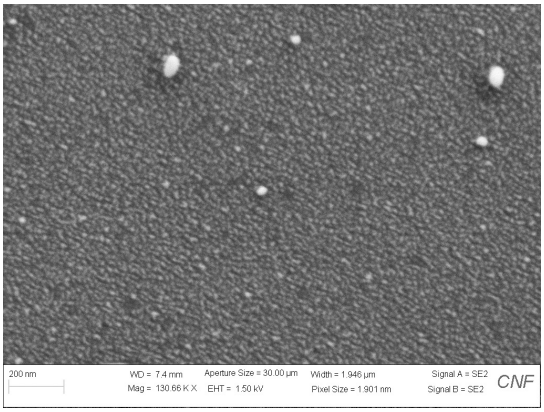

Figure 4: Topography of Al thin film after annealing.

Superconducting Thin Film Growth and Post Laser Annealing

CNF Project Number: 2779-19

Principal Investigator(s): Matthias Liepe

User(s): Zeming Sun

Affiliation(s): Cornell Laboratory for Accelerator-based Sciences and Education, Cornell University

Primary Source(s) of Research Funding: National Science Foundation under Grant No. PHY-1549132

Contact: mul2@cornell.edu, zs253@cornell.edu

Website: https://physics.cornell.edu/matthias-liepe

Primary CNF Tools Used: Oxford FlexAL atomic layer deposition system, Arradiance Gemstar-6 atomic layer deposition system, Woollam spectroscopic ellipsometer, Zygo optical profilometer, P10 profilometer.

Abstract:

Superconducting radio frequency (SRF) cavities are important in accelerating charged particle beams in broad applications such as colliders, neutron sources, and light sources. Niobium tin and magnesium diboride superconductors are the most promising candidates for the next generation SRF cavities. However, their thin film growth is still challenging due to grain boundaries, defects generation, surface roughness, and surface oxidation. Thus, this project investigates the growth mechanisms of superconducting films and explores post processing techniques, such as laser annealing and surface passivation, to mitigate the crystal defects, surface roughness, and oxidation.

Summary of Research:

This report is based on the work done since April 1st, 2019 when Zeming became a user of Cornell NanoScale Science and Technology Facility.

The project has focused on (1) reduction of surface roughness for niobium substrates, (2) deposition and optimization of titanium nitride film as a laser absorber, and (3) deposition of aluminum nitride film for passivating magnesium diboride surface.

(1) Reducing surface roughness of starting niobium substrates is critical for the following deposition of superconducting films since the roughness could negatively affect the nucleation process. Mechanical polishing was exploited, and Zygo optical profilometer was used to monitor the roughness. As shown in Figure 1, the final roughness of niobium substrates are reduced to R_a = 72 nm.

(2) Laser annealing technique has been explored to enable the epitaxial growth of niobium tin grains and also reduce the film surface roughness. Preliminary results showed that niobium tin surface failed to absorb sufficient laser energy using a 120 W, 1064 nm wavelength CO_2 laser and a 250 W, 980 nm wavelength diode laser. In order to enhance the laser light absorption, a titanium nitride film was deposited using thermal atomic layer deposition system. The film thickness and refractive index are important for achieving the anti-reflection. Both parameters were determined by the ellipsometer as shown in Figure 2 and 3.

(3) Magnesium diboride superconducting thin film is easily oxidized in air which hinders its wider application. An aluminum nitride film is deposited on the magnesium diboride film using plasma-enhanced atomic layer deposition. This dielectric film is expected to passivate the magnesium diboride film surface. Further investigations are ongoing.

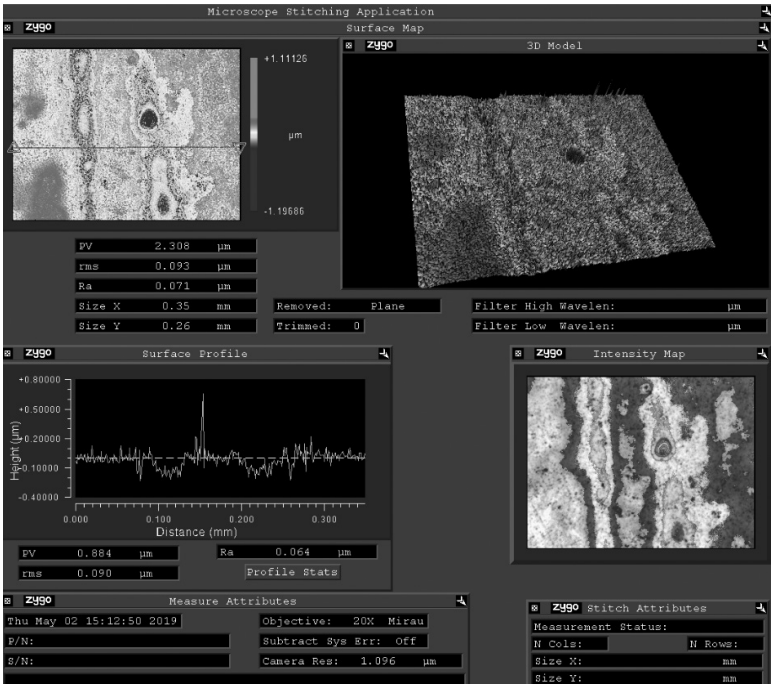

Figure 1: Surface roughness of niobium substrate after mechanical polishing. (Find full color on pages xiv-xv.)

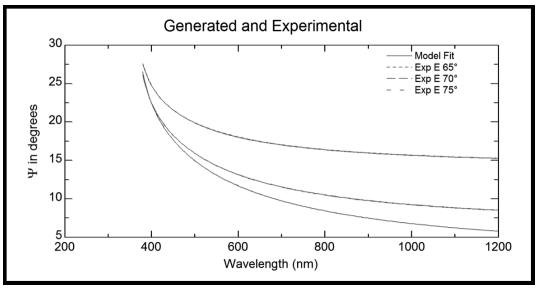

Figure 2: Ellipsometry modeling for determining the thickness of titanium nitride deposited by thermal atomic layer deposition.

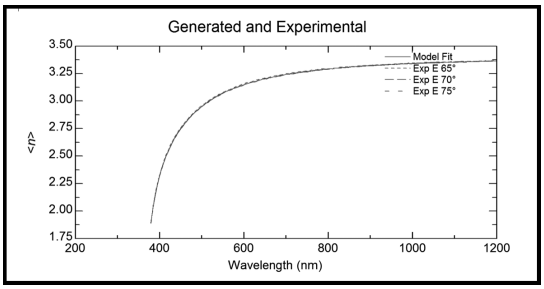

Figure 3: Refractive index of atomic layer deposited titanium nitride film.